VON NEUMANN STABLE, IMPLICIT FINITE VOLUME WENO SCHEMES FOR HYPERBOLIC CONSERVATION LAWS*

TODD ARBOGAST†, CHIEH-SEN HUANG‡, AND XIKAI ZHAO§

Abstract. We present a new approach to defining implicit WENO (iWENO) schemes for systems of hyperbolic conservation laws. The approach leads to schemes that are simple to implement, high order accurate, maintain local mass conservation, apply to general computational meshes, and appear to be fairly robust. We present third and fifth order finite volume schemes in one and two space dimensions. We show that these iWENO schemes are unconditionally stable in the sense of von Neumann stability analysis, assuming the solution is smooth. The solution is approximated efficiently by two or three degrees of freedom per computational mesh element, independent of the spatial dimension. In space, the degrees of freedom are reconstructed implicitly to give high order approximation, while avoiding shocks and steep fronts due to the WENO framework. In time, high order quadrature is employed to produce a one step scheme. The approach is quite general, and we apply it to advection-diffusion-reaction equations with simple diffusion and reaction terms. Numerical results on nonuniform meshes in one and two space dimensions are presented. These explore the properties of the new schemes for solving hyperbolic conservation laws, advection-diffusion equations, advection-reaction equations, and the Euler system.

Key words. implicit WENO scheme, von Neumann stable, hyperbolic conservation law, advection-diffusion-reaction, siWENO

AMS subject classifications. 65M08, 65M12, 76M12

1. Introduction.

Many models in science and engineering involve coupled systems of advection-diffusion-reaction equations

$$u_t + \nabla \cdot [F(u) - D(u)\nabla u] = G(u), \quad x \in \mathbb{R}^d,\ t > 0, \tag{1.1}$$

with a possibly nonlinear flux function $F(u) = F(u; x, t)$, diffusion coefficient $D(u) = D(u; x, t) \geq 0$, and source or reaction term $G(u) = G(u; x, t)$. It is thus important to develop numerical schemes that can approximate all three processes at once. This is quite challenging. When there is a nondegenerate diffusion term throughout the system, the solution is relatively smooth. When diffusion is absent, shocks may form in the solution. When diffusion is present but small, steep fronts in the solution often result, which for numerical purposes look much like shocks. Reactions can change the speed of shocks and steep fronts [32].

In this paper, we develop third and fifth order accurate implicit weighted essentially non-oscillatory (iWENO) numerical schemes to approximate the hyperbolic part

*The work of the first and third authors was supported in part by the U.S. National Science Foundation under grant DMS-1418752. The work of the second author was supported in part by Taiwan Ministry of Science and Technology grant MOST 105-2115-M-110-006-MY2, National Center for Theoretical Sciences, Taiwan, and Multidisciplinary and Data Science Research Center of the National Sun Yat-sen University.

†Department of Mathematics, University of Texas, 2515 Speedway, C1200, Austin, TX 78712-1202 and Institute for Computational Engineering and Sciences, University of Texas, 201 East 24th St., C0200, Austin, TX 78712-1229 (arbogast@ices.utexas.edu)

‡Department of Applied Mathematics, National Sun Yat-sen University, Kaohsiung 804, Taiwan, R.O.C. (huangcs@math.nsysu.edu.tw)

§Department of Mathematics, University of Texas, 2515 Speedway, C1200, Austin, TX 78712-1202 (xzhao@math.utexas.edu)

of this system, i.e., to the system

$$u_t + \nabla \cdot F(u) = 0, \qquad x \in \mathbb{R}^d,\ t > 0, \tag{1.2}$$

$$u(x,0) = u^0(x), \quad x \in \mathbb{R}. \tag{1.3}$$

Being implicit, our schemes are suited to the full equation, and we will consider (1.2) sometimes with the addition of a simple linear, nondegenerate diffusion term and a simple reaction term.

Finite element techniques are well-suited to diffusive processes [10, 17, 6, 14, 8, 5], but they are perhaps less successful handling advection. Finite difference techniques [36, 45] can handle adequately all three processes, but they generally require structured computational meshes. Discontinuous Galerkin methods have become very popular, in part because they can handle all three processes well and can be posed on unstructured meshes [3, 43, 42, 37, 12]. They require a high number of degrees of freedom, and it can be difficult to solve the resulting system of nonlinear equations. Finite volume techniques have similar properties, but have a smaller number of degrees of freedom [30, 32, 48].

Explicit finite difference and finite volume weighted essentially non-oscillatory (WENO) schemes [20, 21, 28, 33, 35, 38] have proven successful for high-order accurate approximation of systems of hyperbolic conservation laws. Being explicit, these schemes are only conditionally stable. When applied to (1.2), the time step Δt must satisfy the CFL condition, which for a uniform rectangular grid of spacing h in d space dimensions may be expressed as $\Delta t \le \Delta t_{\mathrm{CFL}} = C^* h/d$, where C^* is the maximum characteristic speed. However, when second order elliptic diffusion terms are included in the equation, the condition is much more severe: $\Delta t \le Ch^2$ for some constant C.

Many authors have developed implicit or semi-implicit WENO (iWENO) schemes in order to compute solutions to challenging problems (e.g., [9, 49, 7, 22, 47]), and general purpose iWENO schemes have been defined [18, 19]. An iWENO scheme could in principle handle diffusive processes and extend the range of stability beyond the CFL limit. However, practical computations of the hyperbolic equation (1.2) show that these general purpose iWENO schemes achieve only marginal improvement over the CFL time step.

Various Eulerian-Lagrangian (or semi-Lagrangian) schemes have been developed to allow longer time steps than the CFL limit, using either explicit [39, 40, 41, 27, 24, 26] or implicit [25] time stepping. While these schemes achieve their objective, they can be difficult to implement, and so may not be suitable for extension either to problems with diffusion or to high order accuracy.

The locally mass conservative, finite volume iWENO schemes to be developed in this paper use only a few degrees of freedom per computational mesh element, independent of the spatial dimension, making them relatively easy to implement and computationally efficient. The degrees of freedom are reconstructed to give high order approximation in space, while avoiding shocks and steep fronts due to the use of WENO reconstructions. A relatively simple, single step, high order time stepping technique is developed. The schemes are unconditionally stable for smooth solutions in the sense of a von Neumann stability analysis [45], so we designate them as stable iWENO (siWENO) schemes. Preliminary, proof-of-concept tests show the potential generality of the new approach in handling problems with pure advection, advection combined with nondegenerate diffusion, and advection combined with simple reactions, as well as systems of equations and problems in two space dimensions on unstructured meshes. The new scheme appears to be robust for nonlinear problems,

remaining stable even for relatively long time steps.

We do *not* claim to handle the full nonlinear diffusion term nor complex reaction terms. There are subtle interactions between small and/or degenerate diffusion and reactions and advective processes that require further investigation. We plan to study these aspects of the problem in a future work.

The paper is organized as follows. In the next section, we present our siWENO3 and siWENO5 schemes for a scalar equation in one space dimension. For completeness, in Section 3 we describe the WENO reconstructions required for siWENO3. In Section 4, we show that both schemes are unconditionally stable in the sense of von Neumann on uniform grids when applied to the constant coefficient linear equation when it has smooth solutions. We extend the scheme to multiple space dimensions in Section 5, emphasizing the siWENO3 scheme in two space dimensions. We then present numerical results showing the performance of the schemes in one space dimension in Section 6 and the siWENO3 scheme in two space dimensions in Section 7. We close with conclusions.

2. Implicit finite volume WENO scheme in 1D. For simplicity of exposition, we present the basic ideas of our approach for the conservation law in one space dimension. However, for siWENO3, we will include in the equation a diffusion term with a constant coefficient $D \geq 0$ and a simple reaction term, to indicate how these terms can be incorporated. That is, we develop the scheme for the advection-diffusion-reaction equation

$$u_t + \big(f(u) - Du_x\big)_x = g(u), \quad x \in \mathbb{R},\ t > 0. \tag{2.1}$$

Partition space into a grid of points $\cdots < x_{-1} < x_0 < x_1 < \cdots$, and define the element $I_i = [x_i, x_{i+1}]$, its length $\Delta x_i = x_{i+1} - x_i$ and element center $x_{i+1/2} = (x_i + x_{i+1})/2$. Partition time as $0 = t^0 < t^1 < t^2 < \cdots$, and define $\Delta t_n = t^{n+1} - t^n$, $t^{n+1/2} = (t^n + t^{n+1})/2$, and, more generally for use later, $t^{n+\theta} = t^n + \theta \Delta t_n$. For a general function $\phi(x,t)$, we denote

$$\phi_{i+\alpha}^{n+\theta} = \phi(x_i + \alpha \Delta x_i, t^{n+\theta}) \quad \text{for any } \alpha, \theta \in [0,1].$$

The element average of $u(x,t)$ on I_i at time t is

$$\bar{u}_{i+1/2}(t) = \frac{1}{\Delta x_i} \int_{I_i} u(x,t)\, dx.$$

To define a finite volume scheme solving (2.1), we integrate in space over the element I_i, which leads to

$$\frac{d}{dt}\bar{u}_{i+1/2}(t) + \frac{1}{\Delta x_i}\big[\big(\hat{f}_{i+1}(t) - \hat{f}_i(t)\big) - \big(\hat{h}_{i+1}(t) - \hat{h}_i(t)\big)\big] = \frac{1}{\Delta x_i}\int_{I_i} g(u)\, dx, \tag{2.2}$$

where $\hat{f}$ and $\hat{h}$ are numerical fluxes and diffusions, respectively. We take $\hat{f}_i(t) = \tilde{f}(u_i^-(t), u_i^+(t))$, a numerical flux taking into account left and right point values, where $u_i^{\pm}(t) \approx u(x_i^{\pm}, t)$. In fact, we use the Lax-Friedrichs flux, i.e.,

$$\tilde{f}(a,b) = \frac{1}{2}[f(a) + f(b) - \alpha(b-a)], \tag{2.3}$$

where $\alpha = \max_u |f'(u)|$. Since diffusion smooths the solution, we simply use a reconstructed value of u for $\hat{h}_i(t)$, namely,

$$\hat{h}_i(t) = Du_{x,i}(t). \tag{2.4}$$

Moreover, we use the q-point Gaussian quadrature rule to approxmate the integration of the source term, i.e.,

$$\int_{I_i} g(u)\,dx = \Delta x_i \sum_{m=1}^{q} w_m\, g(u(x_{i,m},t)) + \mathcal{O}(\Delta x_i^{2q+1}) \approx \Delta x_i \sum_{m=1}^{q} w_m\, g_{i,m}(t),$$

where $x_{i,m}$ and $\Delta x_i w_m$ are the quadrature points and weights on I_i and $g(u(x_{i,m},t)) = g_{i,m}(t)$. The weak form of (2.2) (in time) is given by multiplying by a test function $v(t)$ and integrating over $[t^n, t^{n+1}]$. After integrating by parts on the left-hand side, we have

$$\begin{aligned} &\bar{u}_{i+1/2}^{n+1} v^{n+1} - \bar{u}_{i+1/2}^{n} v^{n} - \int_{t^n}^{t^{n+1}} \bar{u}_{i+1/2}(t)\, v'(t)\,dt \\ &\quad = -\frac{1}{\Delta x_i}\int_{t^n}^{t^{n+1}} \big[\big(\hat{f}_{i+1}(t) - \hat{f}_i(t)\big) - \big(\hat{h}_{i+1}(t) - \hat{h}_i(t)\big)\big] v(t)\,dt \\ &\qquad + \sum_{m=1}^{q} w_m \int_{t^n}^{t^{n+1}} g_{i,m}(t)\, v(t)\,dt. \end{aligned} \tag{2.5}$$

2.1. A third order, linearly stable, implicit finite volume WENO scheme (siWENO3). In order to get a third order scheme, we need a locally fourth order approximation of the time integral. Recall that Simpson's rule is a locally fifth order approximation, and it is given by

$$\int_{t^n}^{t^{n+1}} \phi(x)\,dx = \frac{\Delta t_n}{6}\big[\phi(t^{n+1}) + 4\phi(t^{n+1/2}) + \phi(t^n)\big] + \mathcal{O}(\Delta t_n^5).$$

First consider $v(t) = v_0(t) = 1$. Applying Simpson's rule to the right-hand side of (2.5), we obtain, up to $\mathcal{O}(\Delta t_n^5/\Delta x_i) + \mathcal{O}(\Delta t_n \Delta x_i^{2q})$,

$$\begin{aligned} &\bar{u}_{i+1/2}^{n+1} - \bar{u}_{i+1/2}^{n} \\ &\quad = -\frac{\Delta t_n}{6\Delta x_i}\Big\{\big[\big(\hat{f}_{i+1}^{n+1} + 4\hat{f}_{i+1}^{n+1/2} + \hat{f}_{i+1}^{n}\big) - \big(\hat{f}_{i}^{n+1} + 4\hat{f}_{i}^{n+1/2} + \hat{f}_{i}^{n}\big)\big] \\ &\qquad\qquad - \big[\big(\hat{h}_{i+1}^{n+1} + 4\hat{h}_{i+1}^{n+1/2} + \hat{h}_{i+1}^{n}\big) - \big(\hat{h}_{i}^{n+1} + 4\hat{h}_{i}^{n+1/2} + \hat{h}_{i}^{n}\big)\big]\Big\} \\ &\qquad + \frac{\Delta t_n}{6}\sum_{m=1}^{q} w_m\big(g_{i,m}^{n+1} + 4g_{i,m}^{n+1/2} + g_{i,m}^{n}\big). \end{aligned} \tag{2.6}$$

Now take $v(t) = v_1(t) = 2(t - t^{n+1/2})/\Delta t_n$, so that $v_1^{n+1} = 1$, $v_1^{n+1/2} = 0$, and $v_1^n = -1$. Applying Simpson's rule to the left-hand side of (2.5), we have

$$\begin{aligned} &\bar{u}_{i+1/2}^{n+1} + \bar{u}_{i+1/2}^{n} - \frac{2}{\Delta t_n}\int_{t^n}^{t^{n+1}} \bar{u}_{i+1/2}(t)\,dt \\ &\quad = \bar{u}_{i+1/2}^{n+1} + \bar{u}_{i+1/2}^{n} - \frac{1}{3}\big(\bar{u}_{i+1/2}^{n+1} + 4\bar{u}_{i+1/2}^{n+1/2} + \bar{u}_{i+1/2}^{n}\big) + \mathcal{O}(\Delta t_n^5) \\ &\quad = \frac{2}{3}\big(\bar{u}_{i+1/2}^{n+1} - 2\bar{u}_{i+1/2}^{n+1/2} + \bar{u}_{i+1/2}^{n}\big) + \mathcal{O}(\Delta t_n^5), \end{aligned}$$

and applying Simpson's rule again to the right-hand side of (2.5), we get, up to $\mathcal{O}(\Delta t_n^5/\Delta x_i) + \mathcal{O}(\Delta t_n^5) + \mathcal{O}(\Delta t_n \Delta x_i^{2q})$,

$$
\begin{aligned}
&4\bar{u}_{i+1/2}^{n+1} - 8\bar{u}_{i+1/2}^{n+1/2} + 4\bar{u}_{i+1/2}^{n} \\
&\quad = -\frac{\Delta t_n}{\Delta x_i}\Big\{\big[(\hat{f}_{i+1}^{n+1} - \hat{f}_{i+1}^{n}) - (\hat{f}_{i}^{n+1} - \hat{f}_{i}^{n})\big] \\
&\qquad\qquad - \big[(\hat{h}_{i+1}^{n+1} - \hat{h}_{i+1}^{n}) - (\hat{h}_{i}^{n+1} - \hat{h}_{i}^{n})\big]\Big\} \\
&\qquad + \Delta t_n \sum_{m=1}^{q} w_m (g_{i,m}^{n+1} - g_{i,m}^{n}).
\end{aligned}
\tag{2.7}
$$

The implicit scheme is given by (2.6) and (2.7), where $\bar{u}_{i+1/2}^{n+1}$ and $\bar{u}_{i+1/2}^{n+1/2}$ are unknowns. We simply use two-point Gaussian quadrature for the reaction term ($q = 2$), which is given by $x_{i,1} = -\sqrt{3}\,\Delta x_i/6 + x_{i+1/2}$, $x_{i,2} = \sqrt{3}\,\Delta x_i/6 + x_{i+1/2}$, and $w_1 = w_2 = 1/2$. Taking $C > 0$ and $\Delta t_n \sim C\Delta x_i$, the scheme has fourth order local truncation error, hence third order global accuracy. Due to the nonlinearity of the system, we use Newton's method to solve for the unknowns. With no source term g, the scheme is locally mass conservative for the total mass at time t^{n+1} by (2.6), and then we see that it is also locally mass conservative for the total mass at time $t^{n+1/2}$ by (2.7).

The point values of u are computed by WENO reconstruction described below in Section 3. We use standard WENO3 (Section 3.1) or WENO-AO(3,2) (Section 3.2) to compute left and right values $u_i^{\pm}(t)$ in the flux terms, WENO-AO(4,3) (Section 3.3) to compute $u_{x,i}(t)$, and WENO-AO(3,2) to compute u at the quadrature points in the reaction term.

Remark. We can extend the siWENO3 scheme to a forth order scheme siWENO4 simply by using higher order WENO reconstructions, e.g., using WENO5 or WENO-AO(5,3) to compute the point values of u and WENO-AO(6,4) to compute $u_{x,i}(t)$.

2.2. A fifth order, linearly stable, implicit finite volume WENO scheme (siWENO5). We begin from (2.5), but we use a higher order quadrature rule for the time integrals and higher order WENO reconstructions in space. We will set $D = 0$ and $g(u) = 0$, since it should be clear from the siWENO3 construction how to add a simple diffusion term and the reaction term. The four point Gauss-Lobatto rule is locally seventh order accurate, and it is given by

$$
\int_{t^n}^{t^{n+1}} \phi(x)\,dx = \frac{\Delta t_n}{12}\big[\phi(t^{n+1}) + 5\phi(t^{n+\theta_2}) + 5\phi(t^{n+\theta_1}) + \phi(t^n)\big] + \mathcal{O}(\Delta t_n^7),
$$

where $\theta_1 = (5 - \sqrt{5})/10$ and $\theta_2 = (5 + \sqrt{5})/10$. Our unknowns will be $\bar{u}^{n+1}$, $\bar{u}^{n+\theta_2}$, and $\bar{u}^{n+\theta_1}$, which gives three per grid element. We will also need three test functions, which must span the space of polynomials of degree 2. We take $v_0 = 1$ and $v_1(t) = 2(t - t^{n+1/2})/\Delta t_n$ as before, and

$$
v_2(t) = \Big(\frac{t - t^n}{\theta_1 \Delta t_n} - 1\Big)\Big(\frac{t - t^n}{\theta_2 \Delta t_n} - 1\Big) = 5\Big(\frac{t - t^{n+1/2}}{\Delta t_n}\Big)^2 - \frac{1}{4}.
$$

Note that

$$v_1^{n+1} = -v_1^n = 1, \quad v_1^{n+\theta_2} = -v_1^{n+\theta_1} = \sqrt{5}/5,$$
$$v_2^{n+1} = v_2^n = 1, \quad v_2^{n+\theta_2} = v_2^{n+\theta_1} = 0,$$
$$v_2'^{,n+1} = -v_2'^{,n} = 5/\Delta t_n, \quad v_2'^{,n+\theta_2} = -v_2'^{,n+\theta_1} = \sqrt{5}/\Delta t_n.$$

We apply the Gauss-Lobatto rule to the time integrals in (2.5) to obtain, up to $\mathcal{O}(\Delta t_n^7) + \mathcal{O}(\Delta t_n^7/\Delta x_i)$, for $v_0(t) = 1$,

$$\begin{aligned} \bar{u}_{i+1/2}^{n+1} - \bar{u}_{i+1/2}^n = -\frac{\Delta t_n}{12\Delta x_i}\Big[&\Big(\hat{f}_{i+1}^{n+1} + 5\hat{f}_{i+1}^{n+\theta_2} + 5\hat{f}_{i+1}^{n+\theta_1} + \hat{f}_{i+1}^n\Big) \\ &- \Big(\hat{f}_i^{n+1} + 5\hat{f}_i^{n+\theta_2} + 5\hat{f}_i^{n+\theta_1} + \hat{f}_i^n\Big)\Big], \end{aligned} \tag{2.8}$$

and for $v_1(t) = (t - t^{n+1/2})/\Delta t_n$,

$$\begin{aligned} &\frac{5}{6}\big(\bar{u}_{i+1/2}^{n+1} - \bar{u}_{i+1/2}^{n+\theta_2} - \bar{u}_{i+1/2}^{n+\theta_1} + \bar{u}_{i+1/2}^n\big) \\ &\quad = -\frac{\Delta t_n}{12\Delta x_i}\Big[\Big(\hat{f}_{i+1}^{n+1} + \sqrt{5}\hat{f}_{i+1}^{n+\theta_2} - \sqrt{5}\hat{f}_{i+1}^{n+\theta_1} - \hat{f}_{i+1}^n\Big) \\ &\qquad\qquad - \Big(\hat{f}_i^{n+1} + \sqrt{5}\hat{f}_i^{n+\theta_2} - \sqrt{5}\hat{f}_i^{n+\theta_1} - \hat{f}_i^n\Big)\Big], \end{aligned} \tag{2.9}$$

and for $v_2(t)$,

$$\begin{aligned} &7\bar{u}_{i+1/2}^{n+1} - 5\sqrt{5}\bar{u}_{i+1/2}^{n+\theta_2} + 5\sqrt{5}\bar{u}_{i+1/2}^{n+\theta_1} - 7\bar{u}_{i+1/2}^n \\ &\quad = -\frac{\Delta t_n}{\Delta x_i}\Big[\Big(\hat{f}_{i+1}^{n+1} + \hat{f}_{i+1}^n\Big) - \Big(\hat{f}_i^{n+1} + \hat{f}_i^n\Big)\Big]. \end{aligned} \tag{2.10}$$

We use either standard WENO5 [28] or WENO-AO(5,3) [4, 2, 11] reconstructions to evaluate the solution in the flux terms.

Taking $C > 0$ and $\Delta t_n \sim C\Delta x_i$, we see that the local truncation error of the scheme is sixth order; hence, the scheme is fifth order accurate globally. Moreover, the scheme is locally mass conservative for the total mass at times $t^{n+\theta_1}$, $t^{n+\theta_2}$, and t^{n+1}. Generalization to higher order schemes should be clear, but we only show our stability result for the third and fifth order schemes.

3. WENO reconstructions in 1D. For the reconstruction of some $x \in I_i$ at a fixed time t from element averages, consider a stencil $S^r \ni I_i$ with r contiguous elements. We can reconstruct u as a stencil polynomial $P^r(x)$ of degree $r-1$ by imposing the conditions

$$\frac{1}{\Delta x_k}\int_{I_k} P^r(x)\,dx = \bar{u}_{k+1/2}, \quad \forall I_k \in S^r.$$

Provided that u is smooth on S^r, P^r is an rth order approximation to u. The smoothness indicator defined by Jiang and Shu [28] is used to measure the smoothness of the polynomial $P^r(x)$ on the element I_i. It is given by

$$\sigma_{P^r} = \sum_{\ell=1}^{r-1}\int_{I_i} \Delta x_i^{2\ell-1}\Big(\frac{d^\ell}{dx^\ell}P^r(x)\Big)^2 dx. \tag{3.1}$$

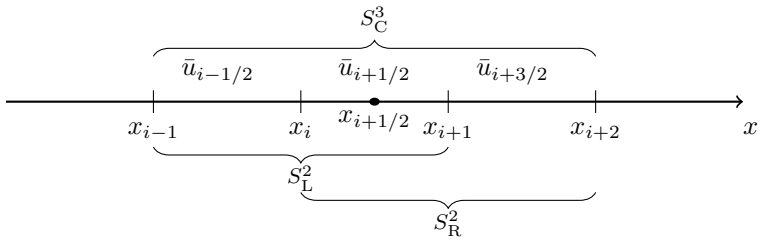

Fig. 3.1: Standard WENO3 stencils.

3.1. Standard WENO3 reconstruction. For a third order standard WENO scheme, we consider the stencils depicted in Figure 3.1, from which two linear polynomials $P^2_{\rm L}$ and $P^2_{\rm R}$, as well as a quadratic polynomial $P^3_{\rm C}$ are reconstructed over $S^2_{\rm L} = \{I_{i-1}, I_i\}$, $S^2_{\rm R} = \{I_i, I_{i+1}\}$, and $S^3_{\rm C} = \{I_{i-1}, I_i, I_{i+1}\}$, respectively.

Given $\hat{x} \in I_i$, we can often find the *exact linear weights* $\alpha^2_{\rm L} > 0$ and $\alpha^2_{\rm R} > 0$ satisfying $\alpha^2_{\rm L} + \alpha^2_{\rm R} = 1$, and

$$P^3_{\rm C}(\hat{x}) = \alpha^2_{\rm L} P^2_{\rm L}(\hat{x}) + \alpha^2_{\rm R} P^2_{\rm R}(\hat{x}).$$

Then, the standard WENO reconstruction [35, 28] is given by the convex combination of the two linear polynomials

$$R_i(\hat{x}) = \tilde{\alpha}^2_{\rm L} P^2_{\rm L}(\hat{x}) + \tilde{\alpha}^2_{\rm R} P^2_{\rm R}(\hat{x}), \tag{3.2}$$

where the *nonlinear weights* $\tilde{\alpha}^2_{\rm L}$ and $\tilde{\alpha}^2_{\rm R}$ are computed by

$$\hat{\alpha}^2_j = \frac{\alpha^2_j}{(\epsilon + \sigma_{P^2_j})^\tau}, \quad \tilde{\alpha}^2_j = \frac{\hat{\alpha}^2_j}{\hat{\alpha}^2_{\rm L} + \hat{\alpha}^2_{\rm R}}, \quad j \in \{\rm L, R\}, \tag{3.3}$$

and we usually take $\tau = 2$ and $\epsilon = 10^{-6}$ to avoid dividing by zero. Note, however, that Aràndiga et al. in [1] suggest taking $\epsilon = K\Delta x_i^2$, for some positive K. The reconstruction is third order accurate when u is smooth, and it drops in order otherwise. For us, $\hat{x}$ is a grid point, so the exact linear weights exist, and we define

$$u^+_i = R_i(x_i) \quad \text{and} \quad u^-_{i+1} = R_i(x_{i+1}). \tag{3.4}$$

3.2. WENO reconstruction with adaptive order (WENO-AO(3,2)). Levy et al. in [34] introduced a compact CWENO3 reconstruction, where they combined the quadratic polynomial with the linear polynomials. Balsara et al. generalized the idea of combining low order polynomials with high order polynomials to define WENO reconstructions with adaptive order [4, 2, 11]. For the third order scheme, we use the same stencil as in Figure 3.1. Define a *centered* polynomial $P^3_{\rm cent}$ such that

$$\alpha^3_{\rm C} P^3_{\rm cent}(x) + \alpha^2_{\rm L} P^2_{\rm L}(x) + \alpha^2_{\rm R} P^2_{\rm R}(x) = P^3_{\rm C}(x),$$

where the *linear weights* $\alpha^3_{\rm C}$, $\alpha^2_{\rm L}$, and $\alpha^2_{\rm R}$ are arbitrary positive numbers summing up to one. We take $\alpha^3_{\rm C} = 1/2$ and $\alpha^2_{\rm L} = \alpha^2_{\rm R} = 1/4$. Then the reconstruction of u at $x \in I_i$ is a convex combination of three polynomials, defined as

$$u(x) \approx R^{\rm AO}_i(x) = \tilde{\alpha}^3_{\rm C} P^3_{\rm cent}(x) + \tilde{\alpha}^2_{\rm L} P^2_{\rm L}(x) + \tilde{\alpha}^2_{\rm R} P^2_{\rm R}(x). \tag{3.5}$$

The *nonlinear weights* $\tilde{\alpha}^3_{\rm C}$, $\tilde{\alpha}^2_{\rm L}$, and $\tilde{\alpha}^2_{\rm R}$ are computed by

$$\hat{\alpha}^s_j = \frac{\alpha^s_j}{(\epsilon + \sigma_{P^s_j})^\tau}, \quad \tilde{\alpha}^s_j = \frac{\hat{\alpha}^s_j}{\hat{\alpha}^3_{\rm C} + \hat{\alpha}^2_{\rm L} + \hat{\alpha}^2_{\rm R}}, \quad j \in \{\text{L, R, C}\}, \quad s \in \{2, 3\}, \tag{3.6}$$

where the constants are usually chosen as $\tau = 2$ and $\epsilon = 10^{-6}$ (but see [2, 11] for consideration of these parameters). One could use $\sigma_{P^3_{\rm cent}}$ in place of $\sigma_{P^3_{\rm C}}$ to define $\hat{\alpha}^3_{\rm C}$.

3.3. WENO reconstruction with adaptive order (WENO-AO(4,3)). We need a reconstruction of u_x when $D \neq 0$. We use the same type of WENO-AO reconstruction to approximate u_x. Note that if u is smooth on S^r, the derivative $P^{r\prime}(x)$ of the rth order stencil polynomial $P^r(x)$ is $(r-1)$st order accurate. Moreover, we wish to maintain spatial symmetry to avoid directional bias in the approximation of the diffusion operator. We therefore use a WENO-AO(4,3) reconstruction, which combines cubic and quadratic polynomials.

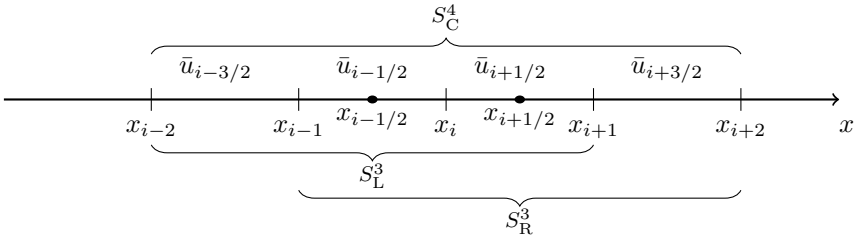

Fig. 3.2: WENO-AO(4,3) stencils.

For a third order reconstruction of the derivative at $x = x_i$, we use the symmetric set of stencils shown in Figure 3.2. Reconstruct a fourth order stencil polynomial $P^4_{\rm C}$ from $S^4_{\rm C} = \{I_{i-2}, I_{i-1}, I_i, I_{i+1}\}$, and two third order polynomials $P^3_{\rm L}$ and $P^3_{\rm R}$ from $S^3_{\rm L} = \{I_{i-2}, I_{i-1}, I_i\}$ and $S^3_{\rm R} = \{I_{i-1}, I_i, I_{i+1}\}$, respectively. Define a *centered* polynomial $P^4_{\rm cent}$ such that

$$\alpha^4_{\rm C} P^4_{\rm cent}(x) + \alpha^3_{\rm L} P^3_{\rm L}(x) + \alpha^3_{\rm R} P^3_{\rm R}(x) = P^4_{\rm C}(x),$$

where the *linear weights* $\alpha^4_{\rm C}$, $\alpha^3_{\rm L}$, and $\alpha^3_{\rm R}$ are arbitrary positive numbers summing up to one. We take $\alpha^4_{\rm C} = 1/2$ and $\alpha^3_{\rm L} = \alpha^3_{\rm R} = 1/4$. Then the reconstruction of u_x at $x \in I_{i-1} \cup I_i$ is a convex combination of three polynomials, defined as

$$u_x(x) \approx R^{\rm AO\prime}_i(x) = \tilde{\alpha}^4_{\rm C} P^{4\prime}_{\rm cent}(x) + \tilde{\alpha}^3_{\rm L} P^{3\prime}_{\rm L}(x) + \tilde{\alpha}^3_{\rm R} P^{3\prime}_{\rm R}(x). \tag{3.7}$$

The *nonlinear weights* $\tilde{\alpha}^4_{\rm C}$, $\tilde{\alpha}^3_{\rm L}$, and $\tilde{\alpha}^3_{\rm R}$ are computed by (3.6), except that now $s \in \{3, 4\}$. Note that we use the smoothness indicators of the polynomials, not their derivatives. These σ depend on which interval we consider x_i belongs, i.e.,

$$\sigma_{P^r} = \sum_{\ell=1}^{r-1} \int_{I_j} \Delta x_j^{2\ell-1} \Big(\frac{d^\ell}{dx^\ell} P^r(x) \Big)^2 dx, \quad j = i-1, i.$$

We take the average of the two choices $j = i-1$ or $j = i$. The derivative is then approximated to third order when u is smooth on $S^4_{\rm C}$. Otherwise, we drop in order of accuracy when the solution is smooth on the center two elements $I_{i-1} \cup I_i$. As is usual in WENO methods, it is not so clear what happens when the discontinuity is within $I_{i-1} \cup I_i$, i.e., no more than an element away from x_i (but we will see that the numerical results show good results).

4. Von Neumann stability analysis of the linear schemes. In this section, we analyze the constant coefficient, linear advection-diffusion-reaction equation,

$$u_t + au_x - Du_{xx} = ru, \quad x \in \mathbb{R},\ t > 0, \tag{4.1}$$

where $a > 0$, $D \geq 0$ and $r \leq 0$. In this case, the Lax-Friedrichs flux (2.3) reduces to the upwind flux, i.e.,

$$\hat{f}_j(t) = \tilde{f}(u_j^-(t), u_j^+(t)) = au_j^-(t) = aR_{j-1}(x_j; t), \quad x_j \in I_{j-1},$$

where the reconstruction R_{j-1} is defined either by (3.2) or (3.5). We assume that the solution u is smooth. WENO methodology then implies that all the nonlinear weights are approximately equal to the linear weights [1, 11, 2], that is, $\tilde{\alpha}_j \approx \alpha_j$, for all j. As a consequence, R_{j-1} evaluates to the quadratic polynomial. We also assume that we have a uniform grid, so $\Delta x_j = h$, for all j.

We apply the von Neumann stability analysis (see, e.g., [45]) to show that the linear scheme is stable for smooth solutions. Consider the kth single Fourier mode $\bar{u}(x,t) = T(t)e^{ikx}$, where in this section i is the canonical imaginary root of -1. Without loss of generality, assume $x_0 = -h/2$, so $x_{j+1/2} = jh$. Then

$$\bar{u}_{j+1/2}(t) = T(t)e^{ikx_{j+1/2}} = T(t)e^{ikjh} = T(t)e^{ij\theta}, \tag{4.2}$$

where $\theta = kh$. We want to show that $|T^{n+1}| \leq |T^n|$.

4.1. Linear stability of siWENO3. We begin with the siWENO3 scheme. Because the WENO nonlinear weights reduce to the linear ones, the reconstruction of the left point value at $x_j \in I_{j-1}$ is

$$u_j^-(t) = R_{j-1}(x_j; t) = P_{\mathrm{C}}^3(x_j) = \frac{1}{6}(-\bar{u}_{j-3/2} + 5\bar{u}_{j-1/2} + 2\bar{u}_{j+1/2}),$$

and, from (3.7),

$$u_{x,j} = R_j^{\mathrm{AO}\prime}(x_j, t) = P_{\mathrm{C}}^{4\prime}(x_j) = \frac{1}{12h}\big(\bar{u}_{j-3/2} - 15\bar{u}_{j-1/2} + 15\bar{u}_{j+1/2} - \bar{u}_{j+3/2}\big).$$

The point values at the reaction quadrature points $x_{j,m} \in I_j$ are

$$\begin{aligned} u(x_{j,1}, t) = R_j(x_{j,1}; t) &= \frac{\sqrt{3}}{12}\bar{u}_{j-1/2} + \bar{u}_{j+1/2} - \frac{\sqrt{3}}{12}\bar{u}_{j+3/2}, \\ u(x_{j,2}, t) = R_j(x_{j,2}; t) &= -\frac{\sqrt{3}}{12}\bar{u}_{j-1/2} + \bar{u}_{j+1/2} + \frac{\sqrt{3}}{12}\bar{u}_{j+3/2}. \end{aligned}$$

The numerical flux terms are

$$\begin{aligned} \hat{f}_{j+1} - \hat{f}_j &= \frac{a}{6}\big[(-\bar{u}_{j-1/2} + 5\bar{u}_{j+1/2} + 2\bar{u}_{j+3/2}) - (-\bar{u}_{j-3/2} + 5\bar{u}_{j-1/2} + 2\bar{u}_{j+1/2})\big] \\ &= \frac{a}{6}\big[\bar{u}_{j-3/2} - 6\bar{u}_{j-1/2} + 3\bar{u}_{j+1/2} + 2\bar{u}_{j+3/2})\big] \end{aligned}$$

and the numerical diffusion terms are

$$\begin{aligned} -\big(\hat{h}_{j+1} - \hat{h}_j\big) &= -\frac{D}{12h}\big[\big(\bar{u}_{j-1/2} - 15\bar{u}_{j+1/2} + 15\bar{u}_{j+3/2} - \bar{u}_{j+5/2}\big) \\ &\qquad - \big(\bar{u}_{j-3/2} - 15\bar{u}_{j-1/2} + 15\bar{u}_{j+1/2} - \bar{u}_{j+3/2}\big)\big] \\ &= \frac{D}{12h}\big[\bar{u}_{j-3/2} - 16\bar{u}_{j-1/2} + 30\bar{u}_{j+1/2} - 16\bar{u}_{j+3/2} + \bar{u}_{j+5/2}\big], \end{aligned}$$

and the reaction terms are $w_1 g_{j,1} + w_2 g_{j,2} = r\bar{u}_{j+1/2}$.

Using (4.2) at a fixed time, we compute that

$$\begin{aligned}\frac{6}{a}T(t)^{-1}e^{-ij\theta}\big(\hat{f}_{j+1}-\hat{f}_j\big) &= e^{-2i\theta}-6e^{-i\theta}+3+2e^{i\theta}\\ &= (\cos\theta - i\sin\theta)^2 - 6(\cos\theta - i\sin\theta)+3+2(\cos\theta+i\sin\theta)\\ &= \cos^2\theta-\sin^2\theta-2i\cos\theta\sin\theta+3-4\cos\theta+8i\sin\theta\\ &= 2-4\cos\theta+2\cos^2\theta+2i\sin\theta(4-\cos\theta)\\ &= 2\,(1-\cos\theta)^2+2i\sin\theta(4-\cos\theta),\end{aligned}$$

which has nonnegative real part, and

$$\begin{aligned}-\frac{12h}{D}T(t)^{-1}e^{-ij\theta}\big(\hat{h}_{j+1}-\hat{h}_j\big) &= e^{-2i\theta}-16e^{-i\theta}+30-16e^{i\theta}+e^{2i\theta}\\ &= 30-32\cos\theta+2(\cos^2\theta-\sin^2\theta)\\ &= 4(1-\cos\theta)(7-\cos\theta),\end{aligned}$$

which is nonnegative. Therefore,

$$T(t)^{-1}e^{-ij\theta}\frac{\Delta t_n}{h}\big[\big(\hat{f}_{j+1}-\hat{f}_j\big)-\big(\hat{h}_{j+1}-\hat{h}_j\big)-\big(w_1g_{j,1}+w_2g_{j,2}\big)\big]=\zeta, \tag{4.3}$$

where ζ is complex and has nonnegative real part (since $r \le 0$).

In terms of (4.2), the kth single Fourier modes at our three time levels are

$$\bar{u}^n_{j+1/2} = T^n e^{ij\theta}, \quad \bar{u}^{n+1/2}_{j+1/2} = T^{n+1/2}e^{ij\theta}, \quad \text{and} \quad \bar{u}^{n+1}_{j+1/2} = T^{n+1}e^{ij\theta}.$$

Substituting these into (2.6) and (2.7), we have that

$$6T^{n+1}-6T^n+\big(T^{n+1}+4T^{n+1/2}+T^n\big)\zeta = 0, \tag{4.4}$$

$$4T^{n+1}-8T^{n+1/2}+4T^n+\big(T^{n+1}-T^n\big)\zeta = 0. \tag{4.5}$$

Multiply (4.4) by 2 and (4.5) by ζ and sum to find that

$$T^{n+1}\big[12+6\zeta+\zeta^2\big]-T^n\big[12-6\zeta+\zeta^2\big]=0.$$

If $\zeta = 0$, then $T^{n+1} = T^n$ and the scheme is stable. If not, we rearrange to obtain

$$T^{n+1}\left[1+\frac{12+\zeta^2}{6\zeta}\right] = T^n\left[-1+\frac{12+\zeta^2}{6\zeta}\right],$$

and we realize that

$$\frac{12+\zeta^2}{6\zeta} = \frac{12\bar{\zeta}+\zeta|\zeta|^2}{6|\zeta|^2} = \mu + i\upsilon$$

has nonnegative real part, i.e., $\mu \ge 0$. Therefore,

$$|T^{n+1}|^2 = |T^n|^2\left|\frac{-1+\mu+i\upsilon}{1+\mu+i\upsilon}\right|^2 = |T^n|^2\frac{(\mu-1)^2+\upsilon^2}{(\mu+1)^2+\upsilon^2} \le |T^n|^2. \tag{4.6}$$

Thus, in terms of von Neumann stability analysis, the scheme is unconditionally stable for the linear equation when u is smooth. It can be shown that the scheme is stable at time $t^{n+1/2}$ (i.e., $|T^{n+1/2}| \le |T^n|$), but we only care about the amplitude at t^{n+1}, since the solution at $t^{n+1/2}$ is *not* used to advance the next step from time t^{n+1} to t^{n+2}.

4.2. Linear stability of siWENO5. From the previous result, it should be clear that a proper, symmetric discretization of diffusion should result in a nonnegative term in the von Neumann stability analysis, as well as the reaction term due to the symmetry of the quadrature points. So we assume $D = 0$ and $r = 0$ in (4.1) for the siWENO5 scheme. Now the standard WENO5 reconstruction at x_j reverts to the value of the fifth order polynomial upstream biased around the center cell I_{j-1}, which is to say,

$$\begin{aligned} u_j^-(t) &= R_{j-1}(x_j;t) = P_{\mathrm{C}}^5(x_j) \\ &= \frac{1}{60}\big(2\bar{u}_{j-5/2} - 13\bar{u}_{j-3/2} + 47\bar{u}_{j-1/2} + 27\bar{u}_{j+1/2} - 3\bar{u}_{j+3/2}\big). \end{aligned}$$

The numerical flux terms are

$$\begin{aligned} \hat{f}_{j+1} - \hat{f}_j &= \frac{a}{60}\big[(2\bar{u}_{j-3/2} - 13\bar{u}_{j-1/2} + 47\bar{u}_{j+1/2} + 27\bar{u}_{j+3/2} - 3\bar{u}_{j+5/2}) \\ &\qquad - (2\bar{u}_{j-5/2} - 13\bar{u}_{j-3/2} + 47\bar{u}_{j-1/2} + 27\bar{u}_{j+1/2} - 3\bar{u}_{j+3/2})\big] \\ &= \frac{a}{60}\big[-2\bar{u}_{j-5/2} + 15\bar{u}_{j-3/2} - 60\bar{u}_{j-1/2} + 20\bar{u}_{j+1/2} + 30\bar{u}_{j+3/2} - 3\bar{u}_{j+5/2}\big]. \end{aligned}$$

Using (4.2) at a fixed time, we compute that

$$\begin{aligned} \frac{60}{a}T(t)^{-1}e^{-ij\theta}\big(\hat{f}_{j+1} - \hat{f}_j\big) &= -2e^{-3i\theta} + 15e^{-2i\theta} - 60e^{-i\theta} + 20 + 30e^{i\theta} - 3e^{2i\theta} \\ &= -2(\cos\theta - i\sin\theta)^3 + 15(\cos\theta - i\sin\theta)^2 - 60(\cos\theta - i\sin\theta) \\ &\quad + 20 + 30(\cos\theta + i\sin\theta) - 3(\cos\theta + i\sin\theta)^2. \end{aligned}$$

The real part of this expression is nonnegative, it being

$$\begin{aligned} &-2(\cos^3\theta - 3\cos\theta\sin^2\theta) + 12(\cos^2\theta - \sin^2\theta) - 30\cos\theta + 20 \\ &\quad = -8\cos^3\theta + 24\cos^2\theta - 24\cos\theta + 8 \\ &\quad = 8(1 - \cos\theta)^3 \geq 0. \end{aligned}$$

Substituting the kth single Fourier modes at our four time levels (4.2) into (2.8)–(2.10), we have that

$$12\big(T^{n+1} - T^n\big) + \big(T^{n+1} + 5T^{n+\theta_2} + 5T^{n+\theta_1} + T^n\big)\zeta = 0, \tag{4.7}$$

$$\begin{aligned} &10\big(T^{n+1} - T^{n+\theta_2} - T^{n+\theta_1} + T^n\big) \\ &\qquad + \big(T^{n+1} + \sqrt{5}T^{n+\theta_2} - \sqrt{5}T^{n+\theta_1} - T^n\big)\zeta = 0, \end{aligned} \tag{4.8}$$

$$7T^{n+1} - 5\sqrt{5}T^{n+\theta_2} + 5\sqrt{5}T^{n+\theta_1} - 7T^n + \big(T^{n+1} + T^n\big)\zeta = 0, \tag{4.9}$$

where ζ has nonnegative real part. Multiply (4.8) by 5 and add it to ζ times (4.9) to discover

$$50\big(T^{n+1} - T^{n+\theta_2} - T^{n+\theta_1} + T^n\big) + 12\big(T^{n+1} - T^n\big)\zeta + \big(T^{n+1} + T^n\big)\zeta^2 = 0.$$

Multiply this by ζ and add to 10 times (4.7), and we have

$$120\big(T^{n+1} - T^n\big) + 60\big(T^{n+1} + T^n\big)\zeta + 12\big(T^{n+1} - T^n\big)\zeta^2 + \big(T^{n+1} + T^n\big)\zeta^3 = 0,$$

which is

$$T^{n+1}\Big[1+\frac{120+12\zeta^2}{60\zeta+\zeta^3}\Big]=T^n\Big[-1+\frac{120+12\zeta^2}{60\zeta+\zeta^3}\Big].$$

Now

$$\frac{120+12\zeta^2}{60\zeta+\zeta^3}=\frac{12(10+\zeta^2)}{\zeta(60+\zeta^2)}=\frac{12\bar\zeta(10+\zeta^2)(60+\bar\zeta^2)}{|\zeta|^2\,|60+\zeta^2|^2},$$

and the real part of the numerator is (after writing $\zeta=\gamma+i\delta$ for real γ and δ, $\gamma\ge 0$)

$$\begin{aligned}&\mathrm{Real}\big[12\bar\zeta(10+\zeta^2)(60+\bar\zeta^2)\big]=\mathrm{Real}\big[12\bar\zeta(600+60\zeta^2+10\bar\zeta^2+|\zeta|^4)\big]\\&\quad=\mathrm{Real}\big[12(\gamma-i\delta)\big(600+70(\gamma^2-\delta^2)+100i\gamma\delta+(\gamma^2+\delta^2)^2\big)\big]\\&\quad=12\big(600+70\gamma^2+30\delta^2+(\gamma^2+\delta^2)^2\big)\gamma\ge 0,\end{aligned}$$

which is nonnegative. Thus (4.6) holds for the siWENO5 scheme, which is then unconditionally stable for the linear equation when u is smooth in terms of von Neumann stability analysis.

5. The scheme in multiple space dimensions. In this section, we extend the scheme to $d>1$ space dimensions. For simplicity, we treat only the siWENO3 scheme. Generalization to siWENO5 should be clear. Partition time in the same way as in Section 2.1, and discretize space by polytopal elements E_k with d-dimensional volume $|E_k|$. Let E_k have L_k facets $\partial E_{k,\ell}$, $\ell=1,\cdots,L_k$ with $|\partial E_{k,\ell}|$ being its $(d-1)$-dimensional volume. The element average of $u(\mathbf{x},t)$ on E_k at time t is

$$\bar u_k(t)=\frac{1}{|E_k|}\int_{E_k}u(\mathbf{x},t)\,dx.$$

For approximation results, we assume that the computational mesh is quasiuniform. Let $h=\max_k|E_k|^{1/d}$ and suppose that $|E_k|=\mathcal{O}(h^d)$ and $|\partial E_k|=\mathcal{O}(h^{d-1})$, with bounds independent of k and ℓ.

5.1. The siWENO3 scheme in multiple space dimensions. Following the semi-discrete finite volume process given in Section 2.1, we integrate (1.1) over the element E_k and apply the Divergence Theorem to obtain

$$\frac{d\bar u_k}{dt}+\frac{1}{|E_k|}\oint_{\partial E_k}(F-D\nabla u)\cdot\nu_k\,ds=\frac{1}{|E_k|}\int_{E_k}G(u)\,dA, \tag{5.1}$$

where ν_k is the outward unit normal of the element boundary ∂E_k. The boundary integral is the sum of the integrals over each facet $\partial E_{k,\ell}$, $\ell=1,\cdots,L_k$. We approximate each such integral using a q-point quadrature rule with points $\mathbf{x}_{k,\ell,m}$ and weights $|\partial E_k|w_{k,\ell,m}$ on facet $\partial E_{k,\ell}$, so the first term in the boundary integral of (5.1) is

$$\oint_{\partial E_k}F\cdot\nu_k\,ds=\sum_{\ell=1}^{L_k}|\partial E_{k,\ell}|\sum_{m=1}^{q}w_{k,\ell,m}\hat F_{k,\ell,m}(t)+\mathcal{O}(h^3), \tag{5.2}$$

where $\hat F_{k,\ell,m}(t)=\hat F\big(u(\mathbf{x}_{k,\ell,m},t)\big)\cdot\nu_k$ is the numerical flux and the quadrature error is assumed to be $\mathcal{O}(h^3)$. We again use the Lax-Friedrichs flux, which is given by

$$\begin{aligned}\hat F_{k,\ell,m}(t)&=\hat F\big(u^-_{k,\ell,m}(t),u^+_{k,\ell,m}(t),\nu_k\big)\\&=\frac{1}{2}\Big[\Big(F\big(u^-_{k,\ell,m}(t)\big)+F\big(u^+_{k,\ell,m}(t)\big)\Big)\cdot\nu_{k,\ell}-\alpha\big(u^+_{k,\ell,m}(t)-u^-_{k,\ell,m}(t)\big)\Big],\end{aligned} \tag{5.3}$$

where α is an upper bound for the absolute value of the eigenvalues of the Jacobian of F in the direction of $\nu_{k,\ell} = \nu_k\big|_{\partial E_{k,\ell}}$, and $u^-_{k,\ell,m}$ and $u^+_{k,\ell,m}$ are reconstructed values of u inside the element and in the neighboring element at the quadrature point $\mathbf{x}_{k,\ell,m}$, respectively. The second term in the boundary integral of (5.1) can be approximated to third order by

$$\oint_{\partial E_k} D\nabla u \cdot \nu \, ds = \sum_{\ell=1}^{L_k} |\partial E_{k,\ell}| \sum_{m=1}^{q} w_{k,\ell,m} \hat{H}_{k,\ell,m}(t) + \mathcal{O}(h^3). \tag{5.4}$$

A reconstructed value $u_{\nu_k,k,\ell,m}(t)$ of $\nabla u(\mathbf{x}_{k,\ell,m}, t) \cdot \nu_k$ is used, so

$$\hat{H}_{k,\ell,m}(t) = \hat{H}\big(u_{\nu_k,k,\ell,m}(t)\big) = D u_{\nu_k,k,\ell,m}(t) \tag{5.5}$$

(D is constant in this paper). Moreover, the integration of the source term $G(u)$ is evaluated to third order by q_E quadrature points over the element E_k, that is,

$$\int_{E_k} G(u) \, dA = |E_k| \sum_{m=1}^{q_E} w_{k,m} G_{k,m}(t) + \mathcal{O}(h^3), \tag{5.6}$$

where $\mathbf{x}_{k,m}$ are the quadrature points, $|E_k| w_{k,m}$ are the corresponding weights, and $G_{k,m}(t) = G(u(\mathbf{x}_{k,m}, t))$.

Now the weak form of (5.1) is

$$\begin{aligned} \int_{t^n}^{t^{n+1}} \frac{d\bar{u}_k}{dt} \, v(t) \, dt + \frac{1}{|E_k|} \int_{t^n}^{t^{n+1}} \oint_{\partial E_k} (F - D\nabla u) \cdot \nu \, v(t) \, ds \, dt \\ = \frac{1}{|E_k|} \int_{t^n}^{t^{n+1}} \int_{E_k} G(u) \, v(t) \, dA \, dt, \end{aligned} \tag{5.7}$$

where $v(t)$ is the test function. We combine (5.7) with (5.2), (5.4), and (5.6). Taking the test functions $v(t) = 1$ and $v(t) = 2(t - t^{n+1/2})/\Delta t_n$, and applying Simpson's rule in time, we get, up to terms of order $\mathcal{O}(\Delta t_n^5) + \mathcal{O}\Big(\Delta t_n^5 \max_\ell |\partial E_{k,\ell}|/|E_k|\Big) + \mathcal{O}(h^3 \Delta t_n)$,

$$\begin{aligned} \bar{u}_k^{n+1} - \bar{u}_k^n = -\frac{\Delta t_n}{6|E_k|} \sum_{\ell=1}^{L_k} |\partial E_{k,\ell}| \sum_{m=1}^{q} w_{k,\ell,m} \Big[\hat{F}^{n+1}_{k,\ell,m} + 4\hat{F}^{n+1/2}_{k,\ell,m} + \hat{F}^n_{k,\ell,m} \\ - \big(\hat{H}^{n+1}_{k,\ell,m} + 4\hat{H}^{n+1/2}_{k,\ell,m} + \hat{H}^n_{k,\ell,m}\big) \Big] \\ + \frac{\Delta t_n}{6} \sum_{m=1}^{q_E} w_{k,m} \big(G^{n+1}_{k,m} + 4G^{n+1/2}_{k,m} + G^n_{k,m}\big) \end{aligned} \tag{5.8}$$

and

$$\begin{aligned} \frac{2}{3}\big(\bar{u}_k^{n+1} - 2\bar{u}_k^{n+1/2} + \bar{u}_k^n\big) \\ = -\frac{\Delta t_n}{6|E_k|} \sum_{\ell=1}^{L_k} |\partial E_{k,\ell}| \sum_{m=1}^{q} w_{k,\ell,m} \Big[\hat{F}^{n+1}_{k,\ell,m} - \hat{F}^n_{k,\ell,m} - \big(\hat{H}^{n+1}_{k,\ell,m} - \hat{H}^n_{k,\ell,m}\big) \Big] \\ + \frac{\Delta t_n}{6} \sum_{m=1}^{q_E} w_{k,m} \big(G^{n+1}_{k,m} - G^n_{k,m}\big), \end{aligned} \tag{5.9}$$

which is our implicit scheme. It is third order if $\Delta t_n = \mathcal{O}(h)$. The value of u at a quadrature point is computed by the WENO-AO reconstruction described in the next section. We use Newton's method to solve the nonlinear system, using the computation of the derivative of the reconstruction with respect to the unknowns $\bar{u}_k^{n+1}$ and $\bar{u}_k^{n+1/2}$ given below in Section 5.3.

When $d = 2$, it is sufficient to take a Gauss quadrature rule with $q = 2$ for the integrals on each edge $\partial E_{k,\ell}$. When an element E_k is a triangle, we can use a $q_E = 3$ Gauss rule, and when the element is a quadrilateral, we can use either a $q_E = 2 \times 2$ Gauss rule mapped from $[-1, 1]^2$ to E_k, or apply two $q_E = 3$ Gauss rules on two triangles bisecting E_k (which is what we do).

5.2. WENO3 reconstruction in 2D. WENO reconstructions on unstructured 2D meshes are developed in [15, 23, 46], and on 3D tetrahedral meshes in [13, 50]. Any of these reconstructions could be used here; however, we choose to develop a reconstruction tailored to logically rectangular meshes of quadrilaterals or cuboidal hexahedra. That is, the mesh is a distortion of a rectangular mesh, and so the index space may be taken to be rectangular. We use a WENO-AO(3,2) reconstruction [34, 4, 2, 11] to combine polynomials that approximate to order three and two (i.e., biquadratics and bilinears). For simplicity, we only describe the reconstruction procedure in 2D. Extension to three (and higher) dimensions is straightforward.

Given an element E_{ij}, let (x_{ij}, y_{ij}) be its centroid. For numerical stability, we also define $h = \sqrt{|E_{ij}|}$ and work in the variables $\xi = (x - x_{ij})/h$ and $\eta = (y - y_{ij})/h$. As shown in Figure 5.1, consider four small stencils S_k^2, $k \in \mathcal{I}_2 = \{\mathrm{SE}, \mathrm{SW}, \mathrm{NE}, \mathrm{NW}\}$, where

$$S_{\mathrm{SE}}^2 = \{E_{ij}, E_{(i+1)j}, E_{i(j-1)}, E_{(i+1)(j-1)}\},\ S_{\mathrm{SW}}^2 = \{E_{ij}, E_{(i-1)j}, E_{(i-1)(j-1)}, E_{i(j-1)}\},$$
$$S_{\mathrm{NE}}^2 = \{E_{ij}, E_{(i+1)j}, E_{i(j+1)}, E_{(i+1)(j+1)}\},\ S_{\mathrm{NW}}^2 = \{E_{ij}, E_{(i-1)j}, E_{(i-1)(j+1)}, E_{i(j+1)}\}.$$

The big stencil is $S_{\mathrm{C}}^3 = \cup_{k \in \mathcal{I}_2} S_k^2$, and we define the full index set $\mathcal{I} = \mathcal{I}_2 + \{\mathrm{C}\}$. We construct the bilinear stencil polynomials P_k^2 from S_k^2 (i.e., on the locally transformed stencil $\hat{S}_k^2$),

$$P_k^2(x, y) = b_0^k + b_1^k \xi + b_2^k \eta + b_3^k \xi\eta, \quad k \in \mathcal{I}_2,$$

and the biquadratic stencil polynomial P_{C}^3 from S_{C}^3 (i.e., $\hat{S}_{\mathrm{C}}^3$),

$$P_{\mathrm{C}}^3(x, y) = a_0 + a_1\xi + a_2\eta + a_3\xi\eta + a_4\xi^2 + a_5\eta^2 + a_6\xi^2\eta + a_7\xi\eta^2 + a_8\xi^2\eta^2,$$

by requiring that each stencil polynomial has the same element average as u for all elements in the corresponding stencil.

For a time dependent problem with a fixed computational mesh, a good way to implement the procedure above is to first define the base polynomials. Given a stencil S with its locally transformed stencil $\hat{S}$, denote the transformed elements as $\hat{E}_{pq} \in \hat{S}$. Let $\hat{\psi}_{pq}$ be the polynomial such that

$$\frac{1}{|\hat{E}_{p'q'}|} \int_{\hat{E}_{p'q'}} \hat{\psi}_{pq}(\xi, \eta)\, d\hat{A} = \begin{cases} 1, & p = p',\ q = q', \\ 0, & \text{otherwise}, \end{cases} \qquad \forall \hat{E}_{p'q'} \in \hat{S}.$$

Note that each $\hat{\psi}_{pq}(\xi, \eta)$ can be precomputed once the mesh is given. The stencil polynomial is then

$$P(x, y) = \hat{P}(\xi, \eta) = \sum_{pq} \bar{u}_{pq} \hat{\psi}_{pq}(\xi, \eta), \quad \forall E_{pq} \in S. \tag{5.10}$$

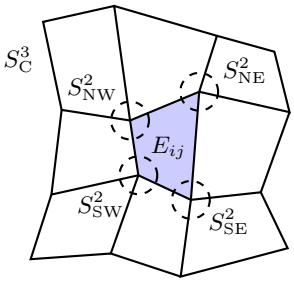

Fig. 5.1: The five stencils for logically rectangular 2D WENO3 reconstruction.

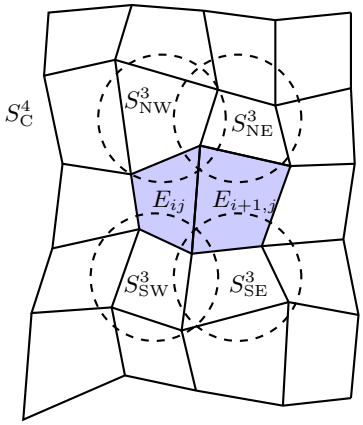

Fig. 5.2: The five stencils for logically rectangular 2D WENO3 reconstruction of the diffusive flux on the interface between E_{ij} and $E_{i+1,j}$.

For any $(x, y) \in E_{ij}$, the third order reconstruction is given by

$$R^{\rm AO}_{ij}(x,y) = \frac{\tilde{\alpha}_{\rm C}}{\alpha_{\rm C}}\Big[P^3_{\rm C}(x,y) - \sum_{k\in\mathcal{I}_2}\alpha_k P^2_k(x,y)\Big] + \sum_{k\in\mathcal{I}_2}\tilde{\alpha}_k P^2_k(x,y), \tag{5.11}$$

where the *linear weights* α_k are arbitrary positive numbers summing up to 1. The *nonlinear weights* $\tilde{\alpha}_j$, $\forall j \in \mathcal{I}$, are computed by

$$\hat{\alpha}_j = \frac{\alpha_j}{(\epsilon + \sigma_{P_j})^\tau}, \quad \tilde{\alpha}_j = \frac{\hat{\alpha}_j}{\sum_{k\in\mathcal{I}}\hat{\alpha}_k}. \tag{5.12}$$

For all the tests in Section 7, we take $\epsilon = |E_{ij}|$, $\alpha_{\rm C} = 1/2$, and $\alpha_j = 1/8$, for all $j \in \mathcal{I}_2$.

The smoothness indicator [23] of the polynomial $P(x, y)$ of degree m is

$$\sigma_P = \sum_{1\le|\alpha|\le m}\int_{E_{ij}} |E_{ij}|^{|\alpha|-1}(\mathcal{D}^\alpha P(x,y))^2 dA, \tag{5.13}$$

where α is a multi-index and $\mathcal{D}$ is the derivative operator. The smoothness indicators

can be computed using the base polynomials (see [1]). For the polynomial P in (5.10),

$$\begin{aligned}
\sigma_P &= \sum_{1\le|\alpha|\le m} |E_{ij}|^{|\alpha|-1} \int_{E_{ij}} (D^\alpha P(x,y))^2 dA \\
&= \sum_{1\le|\alpha|\le m} \int_{\hat{E}_{ij}} (D^\alpha \hat{P}(\xi,\eta))^2 d\hat{A} \\
&= \sum_{1\le|\alpha|\le m} \int_{\hat{E}_{ij}} \Big(\sum_{pq} \bar{u}_{pq} D^\alpha \hat{\psi}_{pq}(\xi,\eta) \Big)^2 d\hat{A} \\
&= \sum_{pq} \sum_{p'q'} \bar{u}_{pq}\, \bar{u}_{p'q'} \sum_{1\le|\alpha|\le m} \int_{\hat{E}_{ij}} D^\alpha \hat{\psi}_{pq}(\xi,\eta) D^\alpha \hat{\psi}_{p'q'}(\xi,\eta)\, d\hat{A} \\
&= \sum_{pq} \sum_{p'q'} \bar{u}_{pq}\, \bar{u}_{p'q'}\, \sigma_{ij,pq}^{p'q'},
\end{aligned} \tag{5.14}$$

where $\sigma_{ij,pq}^{p'q'}$ can be precomputed from the computational mesh.

Evaluation of $G_k^m = G_{ij,m}$ in (5.6) at $\mathbf{x}_{k,m} = \mathbf{x}_{ij,m}$ is straightforward, since only one value for u, $u_{ij,m} = R_{ij}^{\mathrm{AO}}(\mathbf{x}_{ij,m})$, is required. For $\hat{F}_{k,\ell,m} = \hat{F}_{ij,\ell,m}$ in (5.3), the quadrature point lies on a facet between elements, so one reconstructs two values $u_{ij,\ell}^{m,-} = R_{ij}^{\mathrm{AO}}(\mathbf{x}_{ij,\ell,m})$ from center element E_{ij}, and, when the facet is shared by $E_{i'j'}$, $u_{ij,\ell}^{m,+} = R_{i'j'}^{\mathrm{AO}}(\mathbf{x}_{ij,\ell,m})$ from center element $E_{i'j'}$, where $i' = i \pm 1$ and $j' = j$ or $i' = i$ and $j' = j \pm 1$.

Evaluation of normal derivatives for $\hat{H}_{k,\ell,m} = \hat{H}_{ij,\ell,m}$ in (5.5) requires a different reconstruction. To maintain a formal symmetry, we use the stencils depicted in Figure 5.2 to reconstruct a value on the facet between E_{ij} and $E_{i+1,j}$ (a similar construction is used for a facet between E_{ij} and $E_{i,j+1}$). The big stencil of 20 elements is $S_{\mathrm{C}}^4 = \{E_{pq} : i-1 \le p \le i+2,\ j-2 \le q \le j+2\}$ and the small stencils are

$$\begin{aligned}
S_{\mathrm{SE}}^3 &= \{E_{pq} : i \le p \le i+2,\ j-2 \le q \le j\}, \\
S_{\mathrm{SW}}^3 &= \{E_{pq} : i-1 \le p \le i+1,\ j-2 \le q \le j\}, \\
S_{\mathrm{NE}}^3 &= \{E_{pq} : i \le p \le i+2,\ j \le q \le j+2\}, \\
S_{\mathrm{NW}}^3 &= \{E_{pq} : i-1 \le p \le i+1,\ j \le q \le j+2\}.
\end{aligned}$$

The biquadratic polynomials P_k^3, $k \in \{\mathrm{SE}, \mathrm{SW}, \mathrm{NE}, \mathrm{NW}\}$ are constructed by matching the element average of u over each element in the corresponding small stencil, and P_{C} is constructed similarly over the big stencil S_{C}^4, where now P_{C} is 4th order in ξ and 5th order in η. Then

$$R_{\nu_k,ij}^{\mathrm{AO}} = \frac{\tilde{\alpha}_{\mathrm{C}}}{\alpha_{\mathrm{C}}} \Big[\nabla P_{\mathrm{C}}^4(x,y) \cdot \nu_k - \sum_{k\in\mathcal{I}_2} \alpha_k \nabla P_k^3(x,y) \cdot \nu_k \Big] + \sum_{k\in\mathcal{I}_2} \tilde{\alpha}_k \nabla P_k^3(x,y) \cdot \nu_k, \tag{5.15}$$

with nonlinear weighting similar to (5.12)–(5.13). Finally, $u_{\nu_k,k,\ell,m} = R_{\nu_k,ij}^{\mathrm{AO}}$, and we can evaluate $\hat{H}_{ij,\ell,m}$ in (5.5).

5.3. The computation of the derivative of the reconstruction. The Jacobian of the nonlinear system given by (5.8) and (5.9) requires the derivative of R^{AO} at time t^{n+1} or $t^{n+1/2}$ with respect to the unknowns $\bar{u}_k^{n+1}$ or $\bar{u}_k^{n+1/2}$, respectively. This is perhaps the most complicated derivative needed, so we discuss its implementation

here. Fortunately, this derivative is not problem dependent, and so can be coded once for all.

We consider only the derivatives of $R^{\mathrm{AO}}(x,y)$ appearing in (5.11). The derivatives of other reconstructions are computed similarly. Taking the derivative of (5.11), we get

$$\begin{aligned}\frac{\partial R^{\mathrm{AO}}}{\partial \bar{u}_{pq}} &= \frac{P_{\mathrm{C}}^3}{\alpha_{\mathrm{C}}}\frac{\partial \tilde{\alpha}_{\mathrm{C}}}{\partial \bar{u}_{pq}} + \frac{\tilde{\alpha}_{\mathrm{C}}}{\alpha_{\mathrm{C}}}\frac{\partial P_{\mathrm{C}}^3}{\partial \bar{u}_{pq}} \\ &\quad + \sum_{k\in\mathcal{I}_2}\Big[P_k^2\Big(\frac{\partial \tilde{\alpha}_k}{\partial \bar{u}_{pq}} - \frac{\alpha_k}{\alpha_{\mathrm{C}}}\frac{\partial \tilde{\alpha}_{\mathrm{C}}}{\partial \bar{u}_{pq}}\Big) + \Big(\tilde{\alpha}_k - \frac{\tilde{\alpha}_{\mathrm{C}}\alpha_k}{\alpha_{\mathrm{C}}}\Big)\frac{\partial P_k^2}{\partial \bar{u}_{pq}}\Big],\end{aligned} \tag{5.16}$$

so we only need to compute the derivatives of the polynomials and the nonlinear weights. Clearly, if $E_{pq} \notin S_{\mathrm{C}}$, the derivative is zero, so suppose that $E_{pq} \in S_{\mathrm{C}}$. The derivative of a polynomial P, written in the local basis as in (5.10) is

$$\frac{\partial P(x,y)}{\partial \bar{u}_{pq}} = \hat{\psi}_{pq}(\xi,\eta). \tag{5.17}$$

The derivative of $\tilde{\alpha}_j$, $j \in \mathcal{I}$, given in (5.12) is

$$\frac{\partial \tilde{\alpha}_j}{\partial \bar{u}_{pq}} = \frac{1}{\big(\sum_{\ell\in\mathcal{I}}\hat{\alpha}_\ell\big)^2}\Big[\frac{\partial \hat{\alpha}_j}{\partial \bar{u}_{pq}}\sum_{\ell\in\mathcal{I}}\hat{\alpha}_\ell - \hat{\alpha}_j\sum_{\ell\in\mathcal{I}}\frac{\partial \hat{\alpha}_\ell}{\partial \bar{u}_{pq}}\Big], \tag{5.18}$$

where

$$\frac{\partial \hat{\alpha}_j}{\partial \bar{u}_{pq}} = -\frac{\tau\alpha_j}{(\epsilon+\sigma_{P_j})^{\tau+1}}\frac{\partial \sigma_{P_j}}{\partial \bar{u}_{pq}}. \tag{5.19}$$

Finally, the derivative of the smoothness indicator for a polynomial P, written in the form (5.14), is

$$\frac{\partial \sigma_P}{\partial \bar{u}_{pq}} = 2\sum_{p'q'}\bar{u}_{p'q'}\sum_{1\le|\alpha|\le m}\int_{\hat{E}_{ij}} D^\alpha\hat{\psi}_{pq}(\xi,\eta)D^\alpha\hat{\psi}_{p'q'}(\xi,\eta)\,d\hat{A} = 2\sum_{p'q'}\bar{u}_{p'q'}\sigma_{ij,pq}^{p'q'}. \tag{5.20}$$

This completes the description of the computation of the derivative of the reconstruction R^{AO} with respect to its unknown $\bar{u}_{pq}$.

6. Numerical results in 1D. We present several examples of our numerical scheme to test its accuracy and performance. We use either a uniform grid with m elements and $\Delta x_i = h$, or a perturbation of it. The grid points are randomly perturbed within $\pm 25\%$ of h, except the boundary points, to form a nonuniform mesh. When we impose periodic boundary conditions, we do not perturb the first and last few points of the interior non-ghost cells, depending on the number of ghost cells required.

6.1. Tests on hyperbolic equations.

Example 6.1.1. Shu's linear test. We begin with the standard *Shu's linear test* on the equation $u_t + u_x = 0$. It is simply the linear translate of a complicated initial condition. We see excellent results in Fig. 6.1 using 3 times the CFL time step at final time $T = 2$.

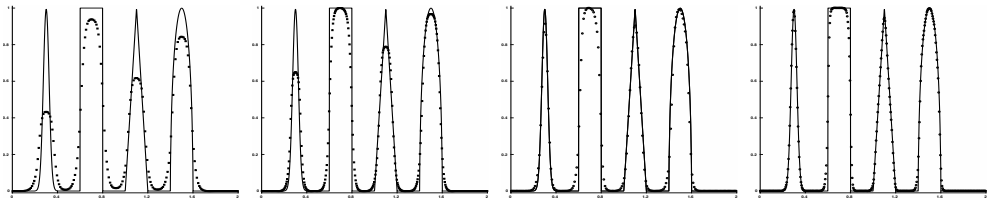

$m = 200$, siWENO3 $m = 400$, siWENO3 $m = 200$, siWENO5 $m = 400$, siWENO5

Fig. 6.1: Example 6.1.1, Shu's linear test. Results are shown at time $T = 2$ for $\Delta t = 3h$ on nonuniform meshes. The solid line is the exact solution.

Example 6.1.2. Burgers equation. We test the schemes on the nonlinear Burgers equation with a simple initial condition to evaluate convergence rates; that is, for the problem

$$u_t + (u^2/2)_x = 0 \quad \text{and} \quad u_0(x) = 0.5 + \sin(\pi x) \quad \text{for} \quad x \in (0, 2).$$

We ran the computation over gradually refined meshes up to time $T = 0.25$, before shocks develop at time $t = 1/\pi \approx 0.32$. The numerical errors and convergence orders for the schemes are given in Tables 6.1–6.2 using uniform and nonuniform meshes, respectively, for various CFL numbers. We see third and fifth order convergence in the L^1-norm (at least when the mesh is fine enough to resolve the nonlinear behavior), even for very long time steps. The L^∞-norm is not as well behaved, but the rates also appear to be optimal in this norm.

Table 6.1: Example 6.1.2, Burgers equation. Error and convergence order at $T = 0.25$ on uniform meshes.

siWENO3					siWENO5				
	L_h^1		L_h^∞			L_h^1		L_h^∞	
m	error	order	error	order	m	error	order	error	order
$\Delta t = 0.5h$									
320	2.29E-05	2.96	1.29E-04	2.76	320	1.18E-06	4.40	3.19E-05	3.83
640	2.89E-06	2.99	1.66E-05	2.96	640	4.13E-08	4.84	1.19E-06	4.74
1280	3.63E-07	3.00	2.09E-06	2.99	1280	1.33E-09	4.96	3.39E-08	4.93
$\Delta t = 5.5h$									
320	4.55E-05	3.08	5.72E-04	2.25	320	9.30E-07	4.56	2.29E-05	4.16
640	4.33E-06	3.39	4.83E-05	3.56	640	3.27E-08	4.83	1.04E-06	4.46
1280	4.69E-07	3.21	4.50E-06	3.42	1280	1.08E-09	4.93	3.40E-08	4.94
$\Delta t = 40.5h$									
640	3.26E-03	2.51	3.32E-02	1.64	640	3.99E-04	3.38	6.55E-03	2.56
1280	3.77E-04	3.11	5.77E-03	2.52	1280	2.22E-05	4.17	5.40E-04	3.60
2560	3.09E-05	3.61	6.07E-04	3.25	2560	6.10E-07	5.18	1.90E-05	4.83

Fig. 6.2 shows the solutions at $T = 3/(2\pi) \approx 0.48$ (after the shocks have formed) with CFL $= 4$. There is no numerical oscillation, and both schemes perform satisfactorily. This is an exceptional result for a non-smooth problem.

Table 6.2: Example 6.1.2, Burgers equation. Error and convergence order at $T = 0.25$ on nonuniform meshes.

siWENO3					siWENO5				
	L_h^1		L_h^∞			L_h^1		L_h^∞	
m	error	order	error	order	m	error	order	error	order
$\Delta t = 0.5h$									
320	2.83E-05	2.90	4.03E-04	1.40	320	1.13E-06	4.45	3.01E-05	3.83
640	3.48E-06	3.03	5.38E-05	2.91	640	4.60E-08	4.62	1.48E-06	4.35
1280	4.35E-07	3.00	6.40E-06	3.07	1280	1.49E-09	4.95	4.64E-08	4.99
$\Delta t = 5.5h$									
320	4.91E-05	2.97	4.84E-04	2.77	320	8.69E-07	4.64	2.16E-05	4.15
640	5.04E-06	3.28	6.49E-05	2.90	640	3.62E-08	4.58	1.06E-06	4.34
1280	5.46E-07	3.21	7.91E-06	3.04	1280	1.23E-09	4.88	3.35E-08	4.99
$\Delta t = 40.5h$									
640	3.27E-03	2.51	3.31E-02	1.66	640	3.99E-04	3.39	6.54E-03	2.58
1280	3.77E-04	3.12	5.76E-03	2.52	1280	2.22E-05	4.17	5.40E-04	3.60
2560	3.09E-05	3.61	6.07E-04	3.25	2560	6.10E-07	5.18	1.90E-05	4.83

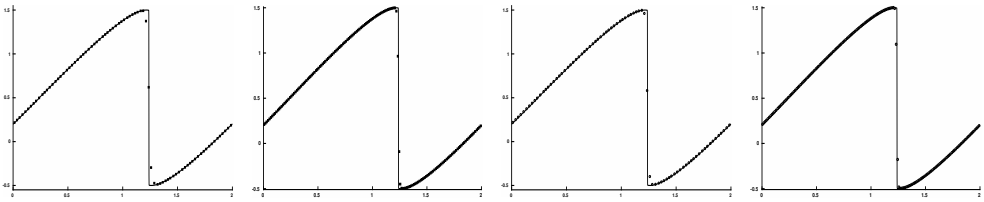

siWENO3, $m = 80$ siWENO3, $m = 160$ siWENO5, $m = 80$ siWENO5, $m = 160$

Fig. 6.2: Example 6.1.2, Burgers equation with a shock. The solution at time $T = 3/(2\pi)$ on nonuniform meshes using CFL = 4. The solid line is the reference solution.

Example 6.1.3. Buckley-Leverett equation. The next example for the scalar equation $u_t + (f(u))_x = 0$ uses the nonconvex Buckley-Leverett flux function

$$f(u) = \frac{u^2}{u^2 + (1-u)^2}. \tag{6.1}$$

The initial condition

$$u_0(x) = \begin{cases} 1 - 20x & \text{for } 0 \le x \le 0.05, \\ 0.5 & \text{for } 0.25 \le x \le 0.4, \\ 0 & \text{otherwise}, \end{cases} \tag{6.2}$$

gives rise to an interaction of shocks and rarefactions, i.e., two pulses merge over time. We use $m = 80$ grid elements. The results for the third order schemes are shown in Fig. 6.3. The schemes handle the merging of the two pulses quite well and reproduce the solution to adequate accuracy even on a relatively low resolution grid.

6.2. Tests on advection-diffusion equations. We now consider the following advection-diffusion equation with linear diffusion,

$$u_t + \big(f(u)\big)_x - Du_{xx} = 0, \quad x \in \mathbb{R},\ t > 0, \tag{6.3}$$

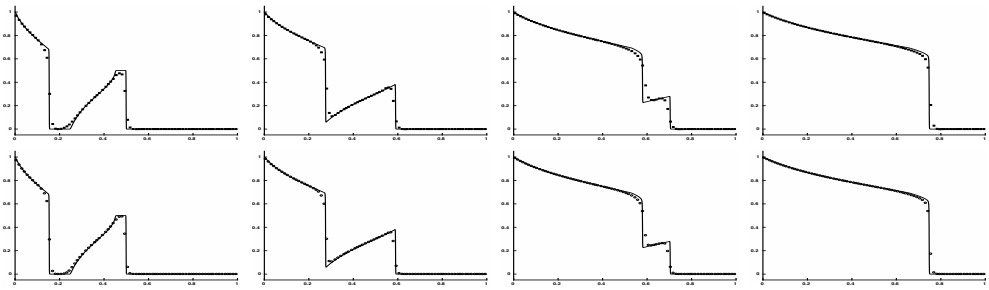

$t = 0.1$, shock and rarefaction formation | $t = 0.2$, initial pulse catches advanced pulse | $t = 0.4$, the two pulses merge | $t = 0.5$, the two pulses are fully merged

Fig. 6.3: Example 6.1.3, Buckley-Leverett. The solid line is the reference solution (CWENO5 with $h = 1/1280$ and $\Delta t = 1/15360$). The squares are siWENO3 (top) and siWENO5 (bottom) results on nonuniform meshes using $m = 80$ and $\Delta t = h$.

where D is assumed to be small, i.e., the equation is advection dominated.

Example 6.2.1. Burgers equation with diffusion. We take $f(u) = u^2/2$ in (6.3). Exact solutions can be found using the Hopf-Cole transformation, and we take the exact solution

$$u(x,t) = \frac{-2D\pi\cos(\pi x)\exp(-D\pi^2 t)}{2 + \sin(\pi x)\exp(-D\pi^2 t)}. \tag{6.4}$$

We show the results for $D = 0.1$ in Table 6.3 on nonuniform grids. Results for uniform grids are very similar. We see the expected convergence rates, except when $\Delta t = 100.5h$, for which we see a higher convergence rate (4 or 6). This is due to the fact that we use Gauss-Lobatto quadrature rules in time, which gives a formal accuracy one power greater in Δt, i.e., the error is $\mathcal{O}(\Delta t^{p+1} + h^p)$ for siWENOp when p is odd. When Δt is large ($\Delta t = 100.5h$), most of the error is in the temporal approximation, and so we see the better convergence rate (but a larger error).

We now take the step function

$$u(x,0) = \begin{cases} a & x < 0.5, \\ b & x > 0.5, \end{cases} \tag{6.5}$$

as initial condition. The exact solution is

$$u(x,t) = a + \frac{b-a}{1 + h(y,t)\exp\left(\frac{b-a}{2D}(y - ct)\right)}, \quad h(y,t) = \frac{1 - \operatorname{erf}\left(\frac{y-at}{\sqrt{4Dt}}\right)}{1 - \operatorname{erf}\left(-\frac{y-bt}{\sqrt{4Dt}}\right)}.$$

where $y = x - 1/2$ and $c = (a+b)/2$. We show the results in Fig. 6.4 with $a = 1$, $b = 0.1$, and $D = 0.03$. The siWENO3 scheme approximates the steep front very well.

6.3. Tests on source or reaction terms.

Example 6.3.1. Burgers equation with nonlinear reaction. We test the nonlinear advection-reaction equation

$$u_t + uu_x = \frac{1}{\tau}u(1-u)(u-\beta),$$

Table 6.3: Example 6.2.1, Burgers with diffusion for (6.4). Errors and convergence order at $T = 2$ for $D = 0.1$ on nonuniform meshes.

siWENO3					siWENO5				
	L_h^1		L_h^∞			L_h^1		L_h^∞	
m	error	order	error	order	m	error	order	error	order
$\Delta t = 0.5h$									
160	7.93E-07	2.96	6.51E-07	2.96	160	4.46E-10	5.14	3.94E-10	5.12
320	9.85E-08	3.01	8.07E-08	3.01	320	1.46E-11	4.94	1.28E-11	4.94
640	1.23E-08	3.00	1.01E-08	2.99	640	4.36E-13	5.06	3.85E-13	5.05
$\Delta t = 10.5h$									
160	6.99E-07	2.76	6.09E-07	2.75	160	4.81E-10	5.38	6.86E-10	5.36
320	9.26E-08	2.92	7.70E-08	2.98	320	1.51E-11	5.00	2.02E-11	5.09
640	1.20E-08	2.95	9.88E-09	2.96	640	4.42E-13	5.09	4.61E-13	5.45
$\Delta t = 100.5h$									
160	7.90E-04	3.52	8.87E-04	3.82	160	3.40E-05	5.76	5.04E-05	5.72
320	5.04E-05	3.97	4.45E-05	4.32	320	4.30E-07	6.31	5.21E-07	6.60
640	3.03E-06	4.05	2.70E-06	4.04	640	6.00E-09	6.16	7.45E-09	6.13

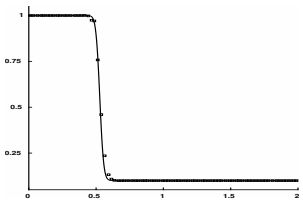

$t = 0.05$, sharp transition region for the shock is immediately smoothed.

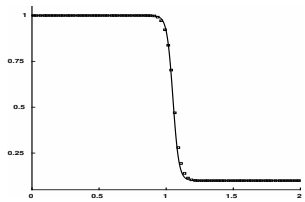

$t = 1$, solution rapidly settles to form a continuously varying transition layer.

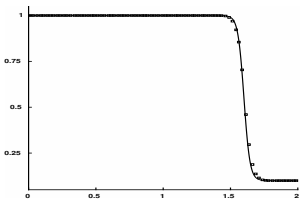

$t = 2$, smoothing effect continues in transition layer between the two step heights.

Fig. 6.4: Example 6.2.1, Burgers equation with diffusion for (6.5). The solid line is the exact solution. The open squares are our siWENO3 scheme with $\Delta t = 2h$ on a nonuniform grid using $m = 80$.

with $\tau = 1/10$, $\beta = 1/4$, initial data $u_0(x) = w\big((x-2)/\tau\big)$, where $w(\xi) = e^\xi/(1+e^\xi)$. The exact solution is $u(x,t) = w\big((x-2-\beta t)/\tau\big)$. As noted by LeVeque [32, §17.15], the solution results from a competition between the transport trying to smear the front to form a rarefaction and the reaction trying to sharpen the front back to the two steady equilibrium points at $u = 0$ and $u = 1$. What develops is a smooth traveling wave moving to the right with speed $\beta = 1/4$. Convergence results are shown in Table 6.4 for the nonuniform mesh over $[0, 4]$, the uniform mesh giving similar results. Optimal convergence is observed, and thus the competition is accurately captured by the siWENO scheme. Figure 6.5 shows the siWENO5 result over $[0, 8]$ using $m = 320$ and $\Delta t = 10h$, and it can be seen that the speed of the traveling wave is $1/4$.

We also ran this test with the opposite initial condition $u_0(x) = w\big(-(x-2)/\tau\big)$, using $m = 320$ over $[0, 8]$ and $\Delta t = 2.5h$. The exact solution rapidly approaches a step function with values 0 and 1, and the shock travels with the Rankin-Hugoniot speed $1/2$ for any value $\beta \in (0, 1)$. The result is shown in Figure 6.5, where indeed the speed of the steep front is $1/2$.

Table 6.4: Example 6.3.1, Burgers equation with reaction, using an initial condition that evolves to a traveling wave moving with speed $\beta = 1/4$. Errors and convergence order on nonuniform meshes over $[0, 4]$ at $T = 1$ with various Δt.

siWENO3					siWENO5				
	L_h^1		L_h^∞			L_h^1		L_h^∞	
m	error	order	error	order	m	error	order	error	order
$\Delta t = h$									
160	2.56E-04	2.92	8.04E-04	2.92	80	4.77E-04	——	2.13E-03	——
320	3.31E-05	2.95	1.15E-04	2.80	160	1.86E-05	4.68	8.39E-05	4.66
640	3.97E-06	3.06	1.56E-05	2.89	320	7.02E-07	4.73	3.07E-06	4.77
$\Delta t = 10h$									
160	2.31E-04	2.92	7.89E-04	2.77	80	4.71E-04	——	2.05E-03	——
320	2.92E-05	2.98	1.09E-04	2.85	160	2.13E-05	4.47	9.73E-05	4.40
640	4.01E-06	2.87	1.71E-05	2.68	320	6.89E-07	4.95	3.09E-06	4.97
$\Delta t = 30h$									
160	1.41E-03	1.74	5.19E-03	1.73	160	1.54E-04	2.63	5.37E-04	2.94
320	1.03E-04	3.77	4.08E-04	3.67	320	3.27E-06	5.55	1.15E-05	5.54
640	8.22E-06	3.65	3.43E-05	3.57	640	7.10E-08	5.53	3.45E-07	5.06

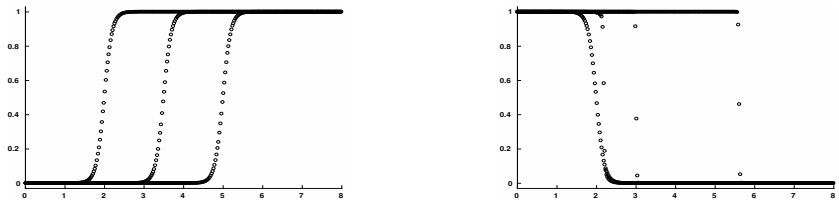

Fig. 6.5: Example 6.3.1. Burgers equation with reaction. Superimposed siWENO5 solutions over $[0, 8]$ using nonuniform meshes and $m = 320$. Left: Traveling wave at times 0, 6 and 12 using $\Delta t = 10h$, showing a speed of $\beta = 1/4$. Right: Sharpening front at times 0, 0.3125, 1.875, and 6.875 using $\Delta t = 2.5h$, showing a shock speed of about $1/2$.

6.4. The Euler system. The incorporation of the eigenspace decomposition and the use of Roe's solver puts stress on the Newton solver, so we incorporated these explicitly by using information from time t^n. Nevertheless, we obtained good solutions to the test problems. We remark that we could incorporate these aspects of the problem fully implicitly but solve them via a quasi-Newton iteration, using values from the previous Newton iteration. Indeed, if we do so, the resolution is a bit better.

Example 6.4.1. A smooth problem for the Euler equations. In this example, the initial condition is set to be $\rho(x, 0) = 1 + 0.2\sin(\pi x)$, $u(x, 0) = 1$, $p(x, 0) = 1$, with 2-periodic boundary conditions. The exact solution is $\rho(x, t) = 1 + 0.2\sin(\pi(x - t))$, $u = 1$, $p = 1$. We compute the solution up to time $T = 2$. The numerical errors and convergence orders for the density are given in Table 6.5.

Example 6.4.2. Riemann problems for the Euler equations. We specify a discontinuous initial condition, written in terms of the primitive variables ρ, u, and p. As is typical, we only report the density ρ; the other variables show comparable

Table 6.5: Example 6.4.1, Euler equations. Error and convergence order for siWENO3 on uniform meshes at $T = 2$.

m	L_h^1 error	order	L_h^∞ error	order
$\Delta t = 3h$				
160	3.26E-04	3.21	9.46E-04	2.50
320	1.96E-05	4.05	6.14E-05	3.95
640	1.05E-06	4.22	2.13E-06	4.85
$\Delta t = 30h$				
160	3.66E-03	3.40	2.95E-03	3.36
320	2.49E-04	3.88	1.90E-04	3.96
640	1.65E-05	3.91	1.29E-05	3.89
$\Delta t = 300h$				
640	8.90E-02	2.04	6.99E-02	2.04
1280	8.56E-03	3.38	6.72E-03	3.38
2560	5.96E-04	3.84	4.68E-04	3.84

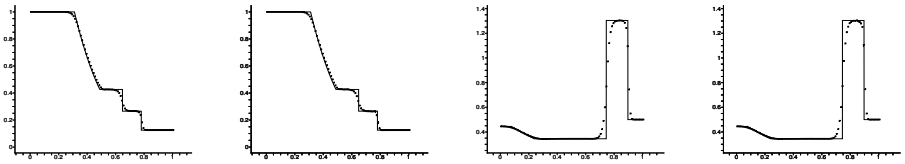

CFL = 2 CFL = 3.5 CFL = 3 CFL = 4.4

Fig. 6.6: Example 6.4.2, Sod and Lax 1-D shock tube tests. The density profile at time $T = 0.16$ for siWENO3 using a uniform grid of $m = 100$ elements.

accuracy. The one-dimensional shock tube test of Sod uses the initial condition

$$\rho, u, p = \begin{cases} \rho_l = 1,\ u_l = 0,\ p_l = 1, & \text{for } x < 1/2, \\ \rho_r = 1/8,\ u_r = 0,\ p_r = 1/10, & \text{for } x > 1/2, \end{cases}$$

and the test of Lax uses the initial condition

$$\rho, u, p = \begin{cases} \rho_l = 0.445,\ u_l = 0.698,\ p_l = 3.528, & \text{for } x < 1/2, \\ \rho_r = 0.5,\ u_r = 0,\ p_r = 0.571, & \text{for } x > 1/2. \end{cases}$$

The results in Fig. 6.6 show the effect of different CFL.

Example 6.4.3. Shu and Osher's shock interaction with entropy waves. In the challenging test case of Shu and Osher [44], a Mach 3 shock interacts with entropy sine waves in the density. We scale the problem to the domain $(0, 1)$, and the initial condition is

$$\rho, u, p = \begin{cases} \rho_l = 3.857143,\ u_l = 2.629369,\ p_l = 10.333333, & \text{for } 0 < x < 1/10, \\ \rho_r = 1 + \epsilon \sin(5(10x - 5)),\ u_r = 0,\ p_r = 1, & \text{for } 1/10 \le x < 1, \end{cases}$$

where $\epsilon = 0.2$. The results at time $T = 0.18$ appear in Fig. 6.7, using $\Delta t = 0.6h$ and $m = 300$, 600 and 900 uniform grid elements. The implicit, third order scheme

siWENO3 tends to smooth the solution, but not as much as the explicit WENO3 scheme (shown for $m = 600$, which gives results between those for siWENO3 using $m = 300$ and $m = 600$).

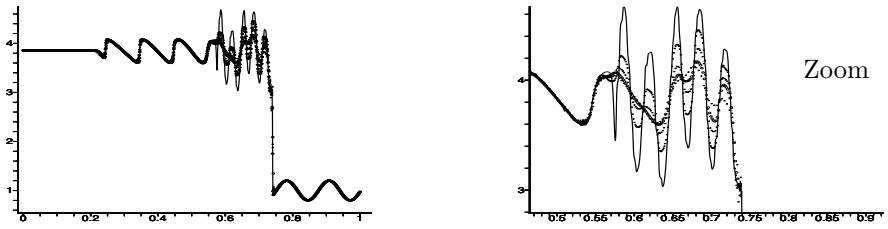

Fig. 6.7: Example 6.4.3, Shu and Osher's test. The density profile for siWENO3 at time $T = 0.18$ using $\Delta t = 0.6h$ and a uniform grid of $m = 300, 600, 900$ elements (small squares). Shown also are results for explicit WENO3 (large circles, $m = 600$, $\Delta t = 0.2h$) and the fine resolution reference solution (solid line).

Example 6.4.4. Woodward and Colella's double blast test. The double blast test of Woodward and Colella uses the initial condition

$$\rho, u, p = \begin{cases} \rho_l = 1,\ u_l = 0,\ p_l = 1000, & \text{for } x < 1/10, \\ \rho_m = 1,\ u_m = 0,\ p_m = 1/100, & \text{for } 1/10 < x < 9/10, \\ \rho_r = 1,\ u_r = 0,\ p_r = 100, & \text{for } 9/10 < x. \end{cases}$$

This is a challenging problem involving the interaction of two shock waves. Nevertheless, reasonably good results are obtained by our siWENO3 scheme using $m = 400$, 800, and 1600 grid elements, as shown in Fig. 6.8, although we need to take a small time step CFL = 0.3. Explicit WENO3 results are also shown for $m = 800$, which compares favorably to siWENO3 at about $m = 600$.

7. Numerical results in 2D. In this section, we give results for siWENO3 in two space dimensions. For all these tests, we impose periodic boundary conditions and use a quadrilateral mesh, which is generated from an $m \times m$ uniform rectangular mesh with edge length h by randomly perturbing the interior points within $\pm 25\%$ of h, except the outer layer (see Figure 7.1 for an example). The outer layer of the elements are not perturbed to facilitate the WENO reconstructions, which require a layer of ghost elements when we use periodic boundary conditions. Newton's method is solved using the sparse direct matrix solver in the Eigen library [16].

Example 7.1. Linear advection. We first test our scheme on linear advection, $u_t + u_x + u_y = 0$ on $[0, 2]^2$, with the initial condition $u(x, y, 0) = \sin(x + y)$. Table 7.1 shows the error and convergence rates at $T = 2$, using $\Delta t = h$, $10h$, and $30h$. We see third order convergence.

Example 7.2. Burgers equation. The next example is a two dimensional Burgers equation

$$u_t + (u^2/2)_x + (u^2/2)_y = 0.$$

We first impose the initial condition

$$u(x, y, 0) = \sin^2(\pi x) \sin^2(\pi y), \quad (x, y) \in [0, 2]^2. \tag{7.1}$$

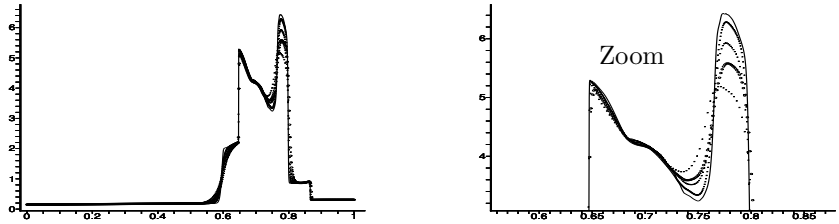

Fig. 6.8: Example 6.4.4, Woodward and Colella's double blast test. The density profile at time $T = 0.038$ on uniform meshes using $m = 400, 800, 1600$ (siWENO3, small squares), $m = 800$ (WENO3, large circles), and $m = 4000$ (MUSCL scheme reference solution, fine line).

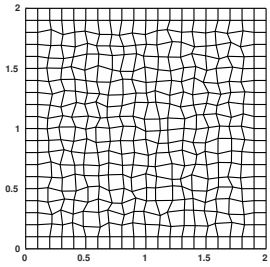

Fig. 7.1: An example of a random perturbation of a 20×20 rectangular mesh.

Table 7.1: Example 7.1. Linear advection in 2D. Error and convergence rate at $T = 2$.

m	L_h^1 error	order	L_h^∞ error	order
$\Delta t = h$				
80	7.6129E-03	2.7965	7.9934E-03	2.1847
160	1.0132E-03	2.9095	1.4827E-03	2.4305
320	1.2637E-04	3.0032	2.3207E-04	2.6756
$\Delta t = 10h$				
80	2.3079E-01	3.2516	9.0695E-02	3.2586
160	1.6119E-02	3.8398	6.5373E-03	3.7879
320	1.0546E-03	3.9340	4.1204E-04	3.9878
$\Delta t = 30h$				
80	4.2561E-00	——	1.6715E-00	——
160	8.9353E-01	2.2519	3.5087E-01	2.2521
320	7.4679E-02	3.5807	2.9346E-02	3.5797

We perturb a 160×160 uniform grid and take $\Delta t = 2h$, corresponding to CFL at least 4. Figure 7.2 shows the results at $t = 0$, 0.75, and 1.5. The scheme resolves the shock well. As we take larger time steps (for example $\Delta t = 3h$), small oscillations appear when the shock first forms, but they disappear after a short time. For very large time steps, we did not get Newton's method to converge.

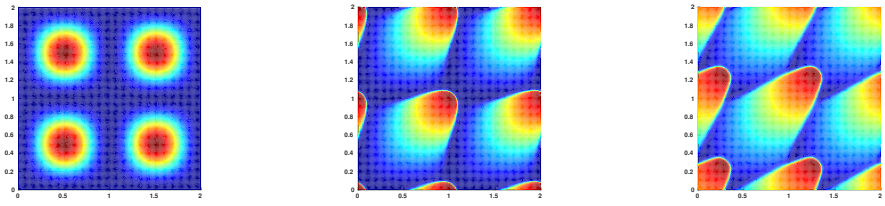

Fig. 7.2: Example 7.2. Burgers equation with initial condition (7.1) using $m = 160$ and $\Delta t = 2h$, at times $t = 0$, 0.75, and 1.5.

Next, we impose a more challenging initial condition given by Jiang and Tadmor [29] involving the "oblique" data given by

$$u(x,y,0) = \begin{cases} 0.5, & x < 0.5, y < 0.5, \\ 0.8, & x > 0.5, y < 0.5, \\ -0.2, & x < 0.5, y > 0.5, \\ -1.0, & x > 0.5, y > 0.5. \end{cases} \tag{7.2}$$

We are interested in the result on $[0,1]^2$. Since we use periodic boundary conditions, we ran the scheme on the larger region $[-0.5, 1.5]^2$, so the interior $[0,1]^2$ is unaffected by the boundary condition. Good results are obtained, as shown in Figure 7.3 on $[0,1]^2$ at $T = 0.5$ on the perturbed 160×160 mesh and $\Delta t = 3h$, with the corresponding CFL $= 6$.

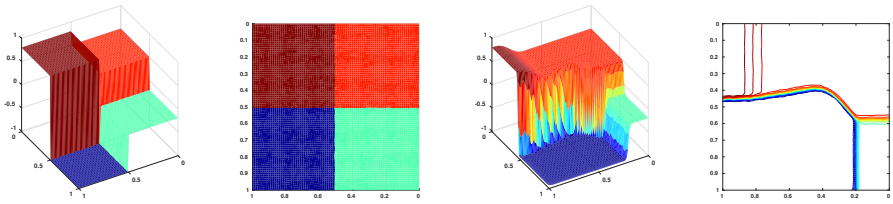

Fig. 7.3: Example 7.2. Burgers equation with "oblique" initial data (7.2) using $m = 160$ and $\Delta t = 3h$ at times $t = 0$ (left two figures) and $t = 0.5$ (right two figures). The contour plot has 21 level lines.

Example 7.3. Rigid body rotation. The equation is

$$u_t - ((y - 1/2)u)_x + ((x - 1/2)u)_y = 0.$$

We consider a rotation of a square patch on $[0,1]^2$. We show the results in Figure 7.4 after a rotation by angle $\pi/4$ and $\pi/2$ using $\Delta t = 2\pi h$. The scheme appears to give good results, even though the mesh is nonuniform. For a large time step such as $\Delta t = 3\pi h$, we see some small oscillations in the first few steps.

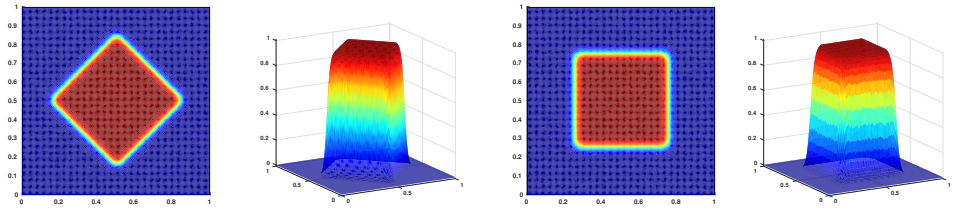

Fig. 7.4: Example 7.3. Rigid body rotation using $m = 160$ and $\Delta t = 2\pi h$ at $t = \pi/4$ (left two figures) and $\pi/2$ (right two figures).

Example 7.4. Swirling flow. The equation is

$$u_t + \left[\sin^2(\pi x)\sin(2\pi y)g(t)u\right]_x - \left[\sin^2(\pi y)\sin(2\pi x)g(t)u\right]_y = 0,$$

where $g(t) = \cos(\pi t/T)$. The initial condition is taken from [31], which contains a slotted disk, a cone, and a smooth hump given by

$$u(x,y,0) = \frac{1}{4}(1+\cos(\pi\, r(x,y))), \quad r(x,y) = \min\left(\sqrt{(x-x_0)^2+(y-y_0)^2}, r_0\right)/r_0,$$

where $x_0 = 0.25$, $y_0 = 0.5$ and $r_0 = 0.15$. The cone and disk have height one and radius 0.15, and they are centered at $(0.5, 0.25)$ and $(0.5, 0.75)$, respectively. We take $\Delta t = 3h$, with 160 elements in each direction. Good results are obtained, as shown in Figure 7.5. At $t = 0.75$, the initial data is of maximum deformation, and at $t = 1.5$, the initial data is recovered. Figure 7.6 shows the second time step with different Δt. We see some oscillations as we take a larger time step, but they all disappear after a few more steps.

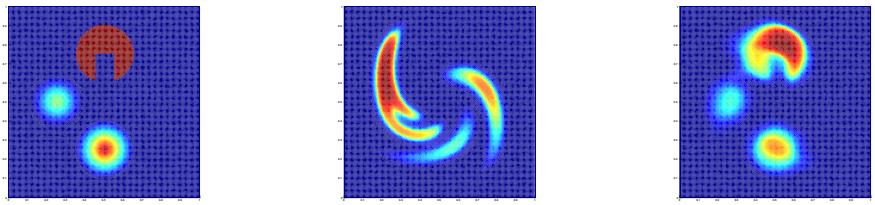

Fig. 7.5: Example 7.4. Swirling flow for $m = 160$ and $\Delta t = 3h$ at $t = 0$, 0.75, and 1.5.

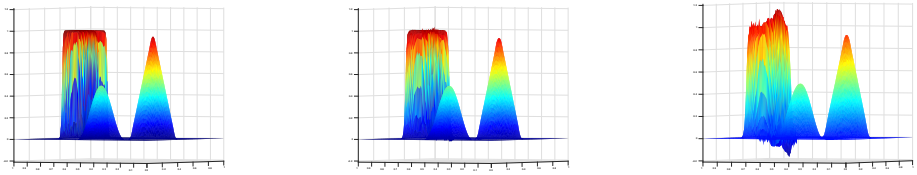

(a) $\Delta t = h$. (b) $\Delta t = 3h$. (c) $\Delta t = 5h$.

Fig. 7.6: Example 7.4. Swirling flow at the second time step t^2 using $m = 160$.

8. Conclusions. We presented a new approach to defining locally conservative, high order, implicit, finite volume WENO schemes for systems of hyperbolic conservation laws. The schemes are unconditionally von Neumann stable for smooth solutions (siWENO schemes). The solution is approximated by its averages over the mesh elements at a few time levels. The keys to high order accuracy are to use WENO reconstruction in space (which handles shocks and steep fronts) combined with a single step, Gauss-Lobatto quadrature in time, and to consider the solution at the advanced quadrature times as unknown. Therefore, the scheme uses only a few degrees of freedom per computational mesh element, independent of the spatial dimension. This makes the scheme fairly computationally efficient, both because reconstructions make use of local information that can fit in cache memory, and because the global system has about as small a number of degrees of freedom as possible. The approach leads to schemes that are simple to implement, high order accurate, maintain local mass conservation, apply to general computational meshes, and appear to be robust.

We presented third and fifth order finite volume schemes in one and two space dimensions. Since our approach is quite general, we applied it to advection-diffusion-reaction equations with simple diffusion and reaction terms. Numerical results on nonuniform meshes in one and two space dimensions showed that the schemes achieve high order accuracy and can take relatively long time steps, on the order of a few CFL to hundreds of CFL, depending on how smooth the solution is. Good results were obtained for solving hyperbolic conservation laws, advection-diffusion equations, advection-reaction equations, and the Euler system.

REFERENCES

[1] F. Aràndiga, A. Baeza, A. M. Belda, and P. Mulet, *Analysis of WENO schemes for full and global accuracy*, SIAM J. Numer. Anal., 49 (2011), pp. 893–915.

[2] T. Arbogast, C.-S. Huang, and X. Zhao, *Accuracy of WENO and adaptive order WENO reconstructions for solving conservation laws*, Submitted, (2017).

[3] I. Babuška, C. Baumann, and J. Oden, *A discontinuous hp finite element method for diffusion problems: 1-d analysis*, Comput. Math. Appl., 37 (1999), pp. 103–122.

[4] D. S. Balsara, S. Garain, and C.-W. Shu, *An efficient class of WENO schemes with adaptive order*, J. Comput. Phys., 326 (2016), pp. 780–804.

[5] D. Braess, *Finite elements: Theory, fast solvers, and applications in solid mechanics*, Cambridge University Press, New York, second ed., 2001.

[6] S. C. Brenner and L. R. Scott, *The Mathematical Theory of Finite Element Methods*, Springer-Verlag, New York, 1994.

[7] A. Cadiou and C. Tenaud, *Implicit WENO shock capturing scheme for unsteady flows. Application to one-dimensional Euler equations*, Int. J. Numer. Meth. Fluids, 45 (2004), pp. 197–229.

[8] Z. Chen, *Finite Element Methods and Their Applications*, Springer-Verlag, Heidelberg and New York, 2005.

[9] Y. J. Chen Y, Yang S, *Implicit weighted essentially non-oscillatory schemes for the incompressible Navier-Stokes equations*, Internat. J. Numer. Methods Fluids, 31 (1999), pp. 747–765.

[10] P. G. Ciarlet, *The Finite Element Method for Elliptic Problems*, North-Holland, Amsterdam, 1978.

[11] I. Cravero, G. Puppo, M. Semplice, and G. Visconti, *CWENO: Uniformly accurate reconstructions for balance laws*, Math. Comp., (2018).

[12] V. Dolejší and M. Feistauer, *Discontinuous Galerkin Method: Analysis and Applications to Compressible Flow*, Springer Series in Computational Mathematics, Springer, 2015.

[13] M. Dumbser and M. Käser, *Arbitrary high order non-oscillatory finite volume schemes on unstructured meshes for linear hyperbolic systems*, J. Comput. Phys., 221 (2007), pp. 693–723.

[14] A. Ern and J.-L. Guermond, *Theory and practice of finite elements*, Applied mathematical sciences, Springer, New York, 2004.

[15] O. Friedrich, *Weighted essentially non-oscillatory schemes for the interpolation of mean values on unstructured grids*, J. Comput. Phys., 144 (1998), pp. 194–212.

[16] G. Gaël, J. Benoît, et al., *Eigen v3*. http://eigen.tuxfamily.org, 2010.

[17] V. Girault and P. A. Raviart, *Finite Element Methods for Navier-Stokes Equations: Theory and Algorithms*, Springer-Verlag, Berlin, 1986.

[18] S. Gottlieb and J. S. Mullen, *An implicit weno scheme for steady-state computation of scalar hyperbolic equations*, in Computational Fluid and Solid Mechanics 2003, K. J. Bathe, ed., vol. 2, Elsevier, 2003, pp. 1946–1950.

[19] S. Gottlieb, J. S. Mullen, and S. J. Ruuth, *A fifth order flux implicit WENO method*, J. Sci. Comput., 27 (2006), pp. 271–287.

[20] A. Harten, B. Engquist, S. Osher, and S. R. Chakravarthy, *Uniformly high-order accurate essentially nonoscillatory schemes III*, J. Comput. Phys., 71 (1987), pp. 231–303.

[21] A. Harten and S. Osher, *Uniformly high-order accurate nonoscillatory schemes I*, SIAM J. Numer. Anal., 24 (1987), pp. 279–309.

[22] T.-J. Hsieh, C.-H. Wang, and J.-Y. Yang, *Simulation of multiple shock-shock interference using implicit anti-diffusive WENO schemes*, Internat. J. Numer. Methods Fluids, 62 (2010), pp. 138–165.

[23] C. Hu and C.-W. Shu, *Weighted essentially non-oscillatory schemes on triangular meshes*, J.

Comput. Phys., 150 (1999), pp. 97–127.
[24] C.-S. Huang and T. Arbogast, *An Eulerian-Lagrangian WENO scheme for nonlinear conservation laws*, Numer. Meth. Partial Diff. Eqns., 33 (2017), pp. 651–680. DOI 10.1002/num.22091.
[25] ———, *An implicit Eulerian-Lagrangian WENO3 scheme for nonlinear conservation laws*, Submitted, (2017).
[26] C.-S. Huang, T. Arbogast, and C.-H. Hung, *A semi-Lagrangian finite difference WENO scheme for scalar nonlinear conservation laws*, J. Comput. Phys., 322 (2016), pp. 559–585. DOI 10.1016/j.jcp.2016.06.027.
[27] C.-S. Huang, T. Arbogast, and J. Qiu, *An Eulerian-Lagrangian WENO finite volume scheme for advection problems*, J. Comput. Phys., 231 (2012), pp. 4028–4052. DOI 10.1016/j.jcp.2012.01.030.
[28] G.-S. Jiang and C.-W. Shu, *Efficient implementation of weighted ENO schemes*, J. Comput. Phys., 126 (1996), pp. 202–228.
[29] G. S. Jiang and E. Tadmor, *Nonoscillatory central schemes for multidimensional hyperbolic conservation laws*, SIAM J. Sci. Comput., 19 (1998), pp. 1892–1917.
[30] R. J. LeVeque, *Numerical Methods for Conservation Laws*, Birkhäuser, Basel, 2nd ed., 1992.
[31] ———, *High-resolution conservative algorithms for advection in incompressible flow*, SIAM. J. Numer. Anal., 33 (1996), pp. 627–665.
[32] ———, *Finite Volume Methods for Hyperbolic Problems*, Cambridge Univ. Press, Cambridge, England, 2002.
[33] D. Levy, G. Puppo, and G. Russo, *Central WENO schemes for hyperbolic systems of conservation laws*, Math. Model. Numer. Anal., 33 (1999), pp. 547–571.
[34] ———, *Compact central WENO schemes for multidimensional conservation laws*, SIAM J. Sci. Comput., 22 (2000), pp. 656–672.
[35] X. D. Liu, S. Osher, and T. Chan, *Weighted essentially non-oscillatory schemes*, J. Comput. Phys., 115 (1994), pp. 200–212.
[36] A. R. Mitchell and D. F. Griffiths, *The Finite Difference Method in Partial Differential Equations*, Wiley, New York, 1980.
[37] D. A. D. Pietro and A. Ern, *Mathematical Aspects of Discontinuous Galerkin Methods*, no. 69 in Mathematiques et Applications Series, Springer, 2012.
[38] J. Qiu and C.-W. Shu, *On the construction, comparison, and local characteristic decomposition for high-order central WENO schemes*, J. Comput. Phys., 183 (2002), pp. 187–209.
[39] J.-M. Qiu and A. Christlieb, *A conservative high order semi-Lagrangian WENO method for the Vlasov equation*, J. Comput. Phys., 229 (2010), pp. 1130–1149.
[40] J.-M. Qiu and C.-W. Shu, *Conservative high order semi-Lagrangian finite difference WENO methods for advection in incompressible flow*, J. Comput. Phys., 230 (2011), pp. 863–889.
[41] ———, *Conservative semi-Lagrangian finite difference WENO formulations with applications to the Vlasov equation*, Communications in Comput. Phys., 10 (2011), pp. 979–1000.
[42] B. Rivière, *Discontinuous Galerkin Methods for Solving Elliptic and Parabolic Equations: Theory and Implementation*, Frontiers in Applied Mathematics, SIAM, 2008.
[43] B. Rivière and M. Wheeler, *A discontinuous Galerkin method applied to nonlinear parabolic equations*, in Discontinuous Galerkin methods, Springer, Berlin, 2000, pp. 231–244.
[44] C.-W. Shu and S. Osher, *Efficient implementation of essentially non-oscillatory shock capturing schemes*, J. Comput. Phys., 77 (1988), pp. 439–471.
[45] J. C. Strikwerda, *Finite Difference Schemes and Partial Differential Equations*, SIAM, Philadelphia, 2nd ed., 2004.
[46] V. A. Titarev, P. Tsoutsanis, and D. Drikakis, *WENO schemes for mixed-element unstructured meshes*, Commun. Comput. Phys., 8 (2010), pp. 585–609.
[47] N. Črnjarić Žic and B. Crnković, *High order accurate semi-implicit WENO schemes for hyperbolic balance laws*, Applied Math. and Computation, 217 (2011), pp. 8611–8629.
[48] H. Versteeg and W. Malalasekera, *An Introduction to Computational Fluid Dynamics: The Finite Volume Method*, Pearson Education Limited, 2 ed., 2007.
[49] J. Yang, Y. Perng, and R. Yen, *Implicit weighted essentially non-oscillatory schemes for the compressible Navier-Stokes equations*, AIAA Journal, 39 (2001), pp. 2082–2090.
[50] Y.-T. Zhang and C.-W. Shu, *Third order WENO scheme on three dimensional tetrahedral meshes*, Commun. Comput. Phys., 5 (2009), pp. 836–848.